Solar Signals in CMIP-5 Simulations: The Ozone Response

L. L. Hood,[a*] S. Misios,[b] D. M. Mitchell,[c] E. Rozanov,[d] L. J. Gray,[c,e] K. Tourpali,[b] K. Matthes,[f,g] H. Schmidt,[h] G. Chiodo,[i] R. Thiéblemont,[f] D. Shindell,[j] A. Krivolutsky,[k]

[a]*Lunar and Planetary Laboratory, University of Arizona, Tucson, Arizona, USA.*

[b]*Laboratory of Atmospheric Physics, Aristotle University of Thessaloniki, Thessaloniki, Greece.*

[c]*Atmospheric, Oceanic and Planetary Physics, University of Oxford, Oxford, UK.*

[d]*Physikalisch-Meteorologisches Observatorium, World Radiation Center, Davos Dorf, Switzerland.*

[e]*NERC, National Centre for Atmospheric Science (NCAS), UK.*

[f]*GEOMAR Helmholtz Centre for Ocean Research Kiel, Kiel, Germany.*

[g]*Christian-Albrechts Universität zu Kiel, Kiel, Germany.*

[h]*Max Planck Institute for Meteorology, Hamburg, Germany.*

[i]*Departamento Fisica de la Tierra II, Universidad Complutense de Madrid, Madrid, Spain.*

[j]*Nicholas School of the Environment, Duke University, Durham, North Carolina, USA.*

[k]*Laboratory for Atmospheric Chemistry and Dynamics, Central Aerological Observatory, Moscow, Russia.*

[*]Correspondence to: Lunar and Planetary Laboratory, University of Arizona, 1629 E. University Blvd., Tucson, Arizona 85721 USA.

E-mail:lon@lpl.arizona.edu

A multiple linear regression statistical method is applied to model data taken from the Coupled Model Inter-Comparison Project, phase 5 (CMIP-5) to estimate the 11-year solar cycle responses of stratospheric ozone, temperature, and zonal wind during the 1979-2005 period. The analysis is limited to the six CMIP-5 models that resolve the stratosphere (high-top models) and that include interactive ozone chemistry. All simulations assumed a conservative 11-year solar spectral irradiance variation based on the NRL SSI model. These model responses are then compared to corresponding observational estimates derived from two independent satellite ozone profile data sets and from ERA Interim Reanalysis meteorological data. The models exhibit a range of 11-year responses with three models (CESM1-WACCM, MIROC-ESM-CHEM, and MRI-ESM1) yielding substantial solar-induced ozone changes in the upper stratosphere that compare more favorably with available observations. The remaining three models do not, apparently because of differences in the details of their radiation and photolysis rate codes. During winter in both hemispheres, the three models with stronger upper stratospheric ozone responses produce relatively strong latitudinal gradients of ozone and temperature in the upper stratosphere that are associated with accelerations of the polar night jet under solar maximum conditions. This behavior is similar to that found in the satellite ozone and ERA Interim data except that the latitudinal gradients tend to occur at somewhat higher latitudes in the models. The sharp ozone gradients are dynamical in origin and assist in radiatively enhancing the temperature gradients, leading to a stronger zonal wind response. These results suggest that simulation of a realistic solar-induced variation of upper stratospheric ozone, temperature and zonal wind in winter is possible for at least some coupled climate models even if a conservative SSI variation is adopted.

Key Words: SolarMIP, solar, stratosphere, ozone, CMIP-5, natural variability

 Prepared using qjrms4.cls

Received . . .

1. Introduction

As reviewed by Mitchell et al. (2014a) (hereafter referred to as Paper 1), the stratosphere containing the ozone layer represents a key link through which solar variability can produce perturbations of tropospheric circulation. Solar influences on surface climate can, in principle, be due either to solar irradiance variations or changes in corpuscular radiation (energetic charged particles), or both (see, e.g., section 4 of the review by Gray et al. 2010). Influences of solar irradiance variability can be further divided into a so-called "bottom-up" category, involving direct penetration of solar radiation at wavelengths greater than about 300 nm to the lower troposphere, and a "top-down" category, involving effects of solar ultraviolet (UV) radiation on the upper atmosphere with indirect dynamical effects at lower levels. Because of the important role of ozone, which is mainly produced by solar UV radiation, in radiatively heating the stratosphere and because solar UV variability is relatively large (up to $\sim$ 6% near 200 nm over an 11-year cycle compared to $\sim$ 0.1% at wavelengths $>$ 300 nm), top-down solar irradiance forcing is believed to be a non-negligible component of solar-induced climate variability (Kodera and Kuroda 2002; Haigh 2003; Matthes et al. 2006; Meehl et al. 2009; Hood et al. 2013; Gray et al. 2013).

There are a number of sources of uncertainty in designing a general circulation model (GCM) that is best able to simulate the observed top-down component of solar irradiance-induced climate change. These include uncertainties in solar spectral irradiance (SSI) variability itself, uncertainties in observational estimates for the solar-induced stratospheric and surface climate response, and uncertainties in the details of the model formulation (see section 2.2 below).

The nature and magnitude of SSI variability has been a topic of increased attention during the last decade. Due to a lack of direct, long-term measurements of SSI, proxy-based models have previously been developed by several groups using indirect measurements such as sunspot area, the solar 10.7 cm radio flux (F10.7), and the solar Mg II core-to-wing ratio (see the review by Ermolli et al. 2013). These SSI models have been extensively employed in climate model simulations. For example, the SSI model developed at the U.S. Naval Research Laboratory (NRL SSI; Lean et al. 1995; Lean 2000; Wang et al. 2005) has been adopted for use by most models in the most recent Coupled Model Intercomparison Project (CMIP-5) (Taylor et al. 2012).

New direct satellite-based measurements of SSI began to be obtained in 2003 by the SORCE (SOlar Radiation and Climate Experiment) (e.g., Harder et al. 2009). As reviewed by Ermolli et al. (2013), the SORCE measurements differ in major ways from the proxy-based models and some of these differences may be a consequence of instrument degradation with time. In particular, a large SSI decrease in the 200 to 320 nm range was measured by SORCE during the decline of solar cycle 23 that was four to six times larger than estimated by proxy-based models. Ermolli et al. (2013) conclude that a lower limit on the magnitude of the SSI solar cycle variation is represented by the NRL SSI model while the SORCE measurements may represent an upper limit. However, results of recent efforts to account for and correct instrument degradation effects in the SORCE SSI data (e.g., Woods 2012) suggest that the measured upper limit will be revised downward considerably.

This is the third in a series of analyses performed as part of the SPARC SOLARIS-HEPPA SolarMIP project (Solar Model Inter-Comparison Project). In Paper 1 (Mitchell et al. 2014a), multiple linear regression (MLR) was applied to assess the 11-year solar cycle component of both stratospheric and surface climate variability in the full suite of more than 30 models that contributed to the CMIP-5 comparison study. The analysis focused on the 13 models that resolve the stratosphere (high-top models) and some evidence was obtained that these models are able to simulate better the surface response during northern winter than are low-top models. However, as a whole, most of the high-top models did not reproduce either the magnitude or latitudinal gradients of solar-induced temperature responses in the upper stratosphere that are estimated using most meteorological reanalyses (see also Mitchell et al. 2014b, in review). For this reason, the high-latitude dynamical responses that lead to significant top-down forcing of regional surface climate were also not well simulated in most of the high-top models. In addition to Paper 1, Misios et al. (2014) have examined the effects of atmosphere-ocean coupling in modifying and enhancing the bottom-up component of solar-induced climate change using both high-top and low-top CMIP-5 models.

In this paper, the model characteristics that yield a reasonable agreement of solar signals with available observations of the stratosphere are examined further. Specifically, multiple linear regression (MLR) is applied to compare in more detail solar signals in a subset of the 13 high-top CMIP-5 models considered in Paper 1, i.e., the 6 models that included coupled interactive ozone chemistry (as opposed to those whose stratospheric ozone variability was prescribed *a priori*). Attention is focused especially on the model response of stratospheric ozone (which was not considered in Paper 1) and comparisons are made to selected observational estimates for the time period after 1979 when continuous global satellite remote sensing measurements began.

In many respects, this study builds on a previous work by Austin et al. (2008; see also Chapter 8 of SPARC-CCMVal 2010). The latter authors analyzed solar cycle signals of ozone and temperature in a series of simulations of coupled chemistry climate models (i.e., general circulation models with coupled interactive chemistry) over various periods during the last half of the 20th century. The employed models did not have coupled oceans but were forced at their lower boundaries using observed sea surface temperatures (SSTs). It was shown that the model ozone results were generally in agreement with observations at tropical latitudes (e.g., Soukharev and Hood 2006), yielding a maximum response near 3-4 hPa of two to three per cent over a solar cycle, a minimum near 20 hPa, and a secondary maximum in the lower stratosphere. The upper stratospheric response is primarily a consequence of increased photolytic ozone production while the lower stratospheric response has a transport origin, resulting from a slowing of the upwelling branch of the mean meridional (Brewer-Dobson) circulation (Kodera and Kuroda 2002). This double-peaked structure was not found to be dependent on whether or not a model included energetic particle precipitation effects or a simulated or prescribed equatorial quasi-biennial wind oscillation (QBO). During the 1960-1981 period, the ozone response maximum in the lower stratosphere was shown to be artificially suppressed due to a fortuitous correlation between the SSTs and the solar cycle. However, during the period from 1982 to 2003, such aliasing was minimal and the lower stratospheric response agreed well with observational estimates over the same period. In the present work, the 6 considered models all have coupled oceans so that aliasing from prescribed SSTs is not a concern and only the period after 1979 is analyzed.

In section 2, the 6 high-top CMIP-5 models with interactive chemistry are described and the MLR statistical method that is applied to the model data is summarized. Results of the analysis for annually averaged monthly solar regression coefficients for stratospheric ozone and temperature are presented and compared for the 6 models. In section 3, previous efforts to estimate observationally the 11-year solar-induced responses of stratospheric ozone, temperature, and zonal wind are first briefly reviewed and selected observations-based estimates for these responses are presented for comparison with the model results. Then the 11-year solar signals in ozone, temperature, and zonal wind for the 6 models are examined in more detail for the northern early winter (Nov.-Dec.) and southern mid-winter (Jul.-Aug.) periods when observations indicate the strongest solar-induced latitudinal gradients in ozone/temperature and the largest enhancements of the polar night jet in both hemispheres. A summary and further discussion are given in section 4.

2. Models, Statistical Method, and Annual Mean Results

2.1. Models

Table I lists the 6 high-top CMIP-5 models with interactive chemistry that are considered here. The institutes that were mainly responsible for producing these models are as follows: CESM1-WACCM - U.S. National Center for Atmospheric Research, Boulder, Colorado; MIROC-ESM-CHEM - University of Tokyo, NIES, and JAMSTEC, Japan; MRI-ESM1 - Meteorological Research Institute of Japan, Tsukuba City, Japan; GFDL-CM3 - U.S. National Oceanic and Atmospheric Administration, Geophysical Fluid Dynamics Laboratory, Princeton, New Jersey; GISS-E2-H and GISS-E2-R - U.S. National Aeronautics and Space Administration, Goddard Institute for Space Studies, New York, New York. The two GISS models differ only in the nature of the coupled ocean model (Shindell et al. 2013). The GISS-E2-R model used the "Russell" ocean (Russell et al. 1995) while the

GISS-E2-H model used the Hybrid Coordinate Ocean Model (Sun and Bleck 2006). All models were required to produce at least one "historical" simulation over the 1850 to 2005 period with observed forcing consisting of solar spectral irradiance variations, volcanic sulfate aerosol, and greenhouse gas emissions (Taylor et al. 2012). Effects of energetic charged particle precipitation were generally not included, except for WACCM, which has a parameterization for increased odd nitrogen production in the thermosphere as a function of the geomagnetic Kp index. All of the models considered here adopted the NRL SSI model (Wang et al. 2005). Two of the models (CESM1-WACCM and GFDL-CM3) also scaled the total solar irradiance (TSI) by a constant factor of 0.9965 to agree with SORCE Total Irradiance Monitor measurements (Kopp et al. 2005).

In the table, column 2 lists the number of ensemble members that were available for analysis for the period after 1979. Three of the models (GFDL-CM3, GISS-E2-H, and GISS-E2-R) were applied to produce an ensemble of 5 historical simulations each. The remaining three (CESM1-WACCM, MIROC-ESM-CHEM, and MRI-ESM1) performed one historical simulation each. In addition, CESM1-WACCM carried out three shorter simulations for the 1955-2005 period with initial conditions taken from the single historical run (Marsh et al. 2013). Therefore, a total of 4 members are available for CESM1-WACCM for the period after 1979 when continuous global satellite observations became available. Column 3 lists the number of bands that represent the solar spectrum in the model's radiation scheme (after Table I of Paper 1). However, the spectral resolution at UV wavelengths is more important for stratospheric ozone production and is discussed in more detail for the individual models in the next subsection. Columns 4 and 5 list the approximate vertical and horizontal spatial resolutions of each model in the stratosphere ($\sim$ 3 hPa). The vertical resolutions at this level are comparable ($\sim$ 2-3 km) for all models except for MIROC-ESM-CHEM, which has a resolution near 1 km. The horizontal resolutions are also comparable (several degrees of latitude or longitude at low latitudes) except for MRI-ESM1, which has a higher resolution near 1 degree. Column 6 indicates whether each model simulates a QBO and whether the modeled QBO is spontaneously generated or whether it is forced (nudged) to agree with observational constraints. Four of the models have no QBO while MIROC-ESM-CHEM has a spontaneous QBO and CESM1-WACCM has a nudged QBO. Finally, column 7 lists at least one recent reference for each model.

2.2. Model Radiation and Photolysis Rate Codes

According to published descriptions, all of the 6 coupled climate models considered here used up-to-date interactive chemistry schemes. The main characteristics of the chemistry schemes for 5 of the 6 models (CESM1-WACCM, MIROC-ESM-CHEM, GFDL-CM3, GISS-E2-R, and GISS-E2-H) have been previously described in detail by Eyring et al. (2013; see their Appendix A). The chemistry scheme used in the MRI-ESM1 model, which provided data to the CMIP-5 archive at a later time, has been summarized by Yukimoto et al. (2010; see also Shibata et al. 2005 and Deushi and Shibata 2010).

However, the modeled response of stratospheric ozone and temperature to 11-year SSI forcing depends strongly on the detailed treatment of the solar UV irradiance in the 120-300 nm spectral range. Experiments using a 1-D radiative-convective-chemical model presented by Shapiro et al. (2013; see their Figure 2) are helpful for demonstrating this. In particular, they showed using the NRL SSI data set that the ozone mixing ratio increases in the stratosphere due to enhanced ozone production by O_2 photolysis with a maximum near 40 km altitude. The increase in the 40-60 km layer is related to O_2 absorption in the 121-200 nm interval (Schumann-Runge bands), while below 40 km the main spectral contribution is from the Herzberg continuum (200-242 nm). A negative ozone response is expected in the middle mesosphere, driven by the increase of hydrogen radicals resulting from water vapor photolysis by SSI in the SRB and at the Lyman-α line. Both the positive ozone response centered near 40 km and the negative response peaking in the middle mesosphere ($\sim$ 68 km) have been confirmed observationally using satellite remote sensing measurements on the solar rotational ($\sim$ 27-day) time scale (e.g., Hood 1986, Keating et al. 1987, Hood et al. 1991). The absorption of SSI at the Lyman-α wavelength by O_2 is also responsible for a strong expected ozone increase in the upper mesosphere. Ozone photolysis in the 240-300 nm spectral range leads to ozone loss partly compensating the influence of enhanced O_2 photolysis above 30 km.

The expected temperature response to an enhancement of solar UV radiation is always positive and has two maxima at the stratopause and mesopause. The mesopause maximum is defined mostly by oxygen absorption in the SRB and in the Lyman-α line. In the 50-70 km layer, the SRB and Herzberg continuum contribution dominates, while below 50 km, ozone absorption in the Herzberg continuum and Hartley bands (200-300 nm) is the main contributor to the overall heating.

For regions where the influence of dynamics is not crucial (e.g., the tropical middle to upper stratosphere and lower mesosphere), differences in modeled ozone and temperature responses to increases in SSI can potentially be explained by different representations of the photolysis and radiative heating responses. Therefore, a detailed consideration of the individual model codes is necessary. It should be noted however that the magnitude of the thermal response depends not only on the details of the shortwave radiation codes but also on the quality of the long-wave part of the codes because the net temperature change is a balance between solar heating and infrared cooling.

<u>CESM1-WACCM</u>

The model version participating in CMIP-5 is described by Marsh et al. (2013). Below 65 km, the heating rates are calculated using the scheme of Briegleb (1992), which is based on the two-stream delta-Eddington approximation. The solar visible and UV (200-700 nm) spectrum is divided into 8 spectral intervals and only ozone absorption, which dominates below 50 km, is taken into account. The photolysis rates are calculated using a look-up table approach based on the output of the Tropospheric Ultraviolet and Visible (TUV) Radiation model developed at NCAR (Madronich and Flocke 1998). Above 65 km, the model also includes parameterizations for the Schumann-Runge bands (Koppers and Murtaugh 1996; Minschwaner and Siskind 1993) and continuum, as well as for the Lyman-α line (Chabrillat and Kockarts 1997). The model is also able to treat extreme UV and X-rays, which are mostly important for the thermosphere. The main weakness of the applied codes is the absence of oxygen absorption below 65 km, which may lead to underestimation of the solar-induced warming and an associated ozone increase there.

<u>MIROC-ESM-CHEM</u>

Radiative heating and photolysis rates are calculated using the radiation code described by Sekiguchi and Nakajima (2008). The radiative transfer solver is based on the two-stream approximation in the form of a discrete-ordinate/adding method and allows treatment of multiple scattering and absorption/emission. The absorption is treated using a correlated k-distribution (CKD) approach. The entire solar spectrum is divided into 23 intervals but the most important ones for the stratosphere/mesosphere solar UV spectrum (185-300 nm) consists of 6 intervals where the absorption by O_3 and O_2 is included. Photolysis rates are calculated on-line using temperature and radiation fluxes computed in the radiation code considering absorption and multiple scattering (Watanabe et al. 2011). The cross-sections and quantum yields of the atmospheric species for each spectral bin are calculated using optimized averaging.

Weaknesses of the applied code include absence of the Lyman-α line and water vapor photolysis. This could potentially lead to some overestimation of the ozone response in the upper stratosphere due to absence of H_2O photolysis in the SRB. At altitudes above 60 km, the neglect of the Lyman-α line would result in problems in the simulation of both the ozone and temperature responses.

<u>MRI-ESM1</u>

The model version participating in CMIP-5 is described by Adachi et al. (2011). The calculation of heating rates in this version is performed with the two-stream delta-Eddington approximation with the entire solar spectrum divided into 22 spectral intervals (Yukimoto et al. 2011, 2012). The absorption of solar UV radiation by O_2 and O_3 is included following Freidenreich and Ramaswamy (1999), which divides the spectrum from 173 to 400 nm into 11 intervals. Absorption in the molecular lines is treated using a CKD approach. The photolysis rate calculation is based on the scheme applied in the NCAR 2-D model SOCRATES (Huang et al. 1998) and includes all reactions important for the stratosphere and mesosphere. The only obvious weakness of the radiation code is the absence of the Lyman-α line.

GFDL-CM3

The model version participating in CMIP-5 is described by Donner et al. (2011). The applied radiation code is based on an original algorithm presented by Freidenreich and Ramaswamy (1999). To improve performance, the code was slightly simplified by reducing the total number of spectral intervals covering the solar spectrum from 25 to 18. However, in the UV range (173-300 nm), the number of intervals remains the same as in the original scheme (Anderson et al. 2004). Clear-sky photolysis rates are calculated using a multivariate interpolation table derived from the TUV model of Madronich and Flocke (1998), with an adjustment applied for the effects of large-scale clouds. As in MRI-ESM1, the only obvious weakness of the radiation code is the absence of the Lyman-α line. However, it appears that the applied photolysis rate calculation scheme was designed mostly for tropospheric applications so it is possible that O_2 photolysis could be missing because this reaction is not important in the troposphere.

GISS-E2-H and GISS-E2-R

The model versions participating in CMIP-5 are described by Schmidt et al. (2014). As noted in section 2.1, the H and R versions differ only in the nature of the coupled ocean model. The calculation of heating rates is based on the Lacis and Hansen (1974) parameterization, which considers solar UV absorption only by ozone. The photolysis rates are calculated using the Fast_J2 code of Bian and Prather (2002), which takes into account the model distribution of clouds, aerosols, and ozone. The scheme was improved by adding photolysis of water and NO at high altitudes. The weakness of the applied radiation code is absence of oxygen absorption, which is very important in the upper stratosphere/mesosphere. The absence of the SRB and Lyman-α line in the Fast-H2 code could also lead to an underestimation of the positive ozone and temperature response above 40 km. This underestimation could be enhanced by the added photolysis of water vapor, which provides additional active hydrogen during solar maximum years.

2.3. Method of Analysis

As in Paper 1, we adopt here a multiple linear regression (MLR) statistical approach to estimate the 11-year solar component of variability in the model ozone, temperature, and zonal wind monthly mean time series. Because the solar signal evolves significantly as a function of season, monthly solar regression coefficients are calculated for comparison to corresponding observational estimates described in section 3. The MLR model applied here differs from that applied in Paper 1 only in that the adopted solar predictor (basis function) is the solar Mg II core-to-wing ratio (or Mg II UV index), which is available since 1979 when continuous satellite measurements of SSI began. This index, which consists of a ratio that is insensitive to instrument-related drifts, is a measure of solar UV variations at wavelengths near 200 nm that are important for ozone production in the upper stratosphere (Heath and Schlesinger 1986; Viereck and Puga 1999). It is demonstrably more effective (see below and Figure S7) in representing solar-induced signals in observational stratospheric ozone data than other proxies such as total solar irradiance (TSI), F10.7, or sunspot number. In Paper 1, for the purpose of analyzing model stratospheric temperature and zonal wind data, the NRL model TSI was adopted as the solar basis function because it, unlike Mg II, is available for the full historical period (1850-2005) and because the UV component of SSI was not represented uniformly in all of the CMIP-5 models.

Specifically, the adopted MLR model for a given atmospheric variable and month $X(i,t)$ is of the form:

$$\begin{aligned} X(i,t) &= \mu(i) + \beta_{\rm solar}{\rm MgII}(i,t) + \beta_{\rm volcanic}{\rm SATO}(i,t) \\ &+ \beta_{\rm QBO1}{\rm QBO1}(i,t) + \beta_{\rm QBO2}{\rm QBO2}(i,t) \\ &+ \beta_{\rm ENSO}{\rm N3.4}(i,t) + \beta_{\rm trend}{\rm GHG}(i,t) + {\rm r}(i,t) \qquad (1) \end{aligned}$$

where i is the month of the year (i = 1, 2, ..., 12), t is the time in increments of years, $\mu(i)$ is the long-term mean for the ith month, Mg II(i,t) is the corresponding value of the Mg II UV index, available from the Laboratory for Atmospheric and Space Physics at the University of Colorado (http://lasp.colorado.edu/lisird/mgii), SATO(i,t) is a measure of the volcanic aerosol concentration (updated from Sato et al. 1993), QBO1(i,t) and QBO2(i,t) are the first and second Empirical

Orthogonal Functions of the model equatorial (5°S to 5°N) zonal mean zonal wind at levels from 5 to 70 hPa in the stratosphere, N3.4(i, t) is the Niño 3.4 index (defined as the model sea surface temperature anomalies in the region from 5°S to 5°N and from 120°W to 170°W), GHG(i, t) is a time series representative of the concentration of well-mixed greenhouse gases, and r(i, t) is the residual noise term. The coefficients $\beta_{\rm solar}$, $\beta_{\rm volcanic}$, $\beta_{\rm QBO1}$, $\beta_{\rm QBO2}$, $\beta_{\rm ENSO}$, and $\beta_{\rm trend}$ are determined by linear least squares regression. Note that the QBO1, QBO2, and N3.4 basis function time series must be calculated from the model data for each individual model prior to application of (1). For models with no QBO, the QBO terms are set to zero. As described in more detail in Paper 1, to correct for autocorrelation of the model data residuals after applying (1), we use the method of Tiao et al. (1990) (see also Cochrane and Orcutt 1949 and Garny et al. 2007). However, the correction is relatively minor since the year-to-year autocorrelation of the monthly residuals is not large.

2.4. *Annual Mean Model Results*

Figure 1 shows annual averages of the monthly solar regression coefficients calculated from model ozone data over the 1979-2005 period for all 6 models listed in Table 1. These averages are produced by first calculating the monthly regression coefficients and standard deviations for each ensemble member for a given model (4 for CESM1-WACCM, 1 for MIROC-ESM-CHEM, 1 for MRI-ESM1, and 5 each for GFDL-CM3, GISS-E2-H, and GISS-E2-R). The ensemble means are then calculated for each model and month (see Figures S1-S6). Finally, the ensemble means of the coefficients and standard deviations for each of the 12 months are averaged together for each model at each grid point to produce Figure 1. The starting point of 1979 is determined by the beginning of continuous satellite observations (section 3) while the end point of 2005 is determined by the final year of the CMIP-5 simulations. Ozone regression results are only shown at altitudes above 16 km since the vast majority of the ozone column is in the stratosphere. Results are not shown above 54 km since 4 of the 6 models only provide data to approximately this level.

Ozone solar regression coefficients are expressed as the per cent change in ozone concentration or mixing ratio for a change in the Mg II core-to-wing ratio of 0.0169. The latter value is roughly equivalent to a change in F10.7 of $\sim$ 130 flux units or a change in sunspot number of $\sim$ 130, i.e., it corresponds to a cycle that is about average for the 1940-2000 period but stronger-than-average for the 1850-1940 period. In the remainder of this paper, this change is referred to as solar "minimum to maximum" or "max - min". In this and subsequent figures, dark shaded areas indicate regions where the averaged monthly solar regression coefficients are greater than twice the averaged monthly standard deviations. These areas are statistically significant at approximately 95% confidence. Lighter shaded areas indicate regions where the coefficients are more than one averaged monthly standard deviation and are significant at approximately 68% confidence.

Figures S1-S6 show the monthly ensemble mean ozone solar regression coefficients for each of the 6 models that were averaged together to produce the annually averaged plots in Figure 1. Figure S7 confirms that the Mg II solar UV index gives more significant ozone solar coefficient regression results for the CMIP-5 model ozone data over the 1979-2005 period. It compares the annually averaged monthly ozone solar regression coefficients obtained for the CESM1-WACCM model when the assumed solar basis function consists of (a) TSI; (b) F10.7; and (c) the solar Mg II UV index. Both the amplitude and statistical significance of the solar regression coefficients are largest when the Mg II UV index is used. Nevertheless, the TSI index used in Paper 1 for atmospheric variables other than ozone over the 1850-2005 period remains a valid solar proxy.

As seen in Figure 1, there is a wide range in the amplitude and statistical significance of the ozone solar regression results among the models, especially in the upper stratosphere. Despite the short 27-year analysis period, statistically significant solar coefficients are obtained for 5 of the 6 models. Results for models with little or no response in the upper stratosphere are shown in the lower panel (Figure 1 d, e, and f). Overall, the least significant coefficients were obtained for GFDL-CM3 while the most significant coefficients were obtained for MRI-ESM1. The GFDL-CM3 results are not significant at the 2σ level with only marginally significant (1σ) values obtained in the lower stratosphere. The two GISS-E2 models produce a significant ozone response with maximum averaged amplitude of $\sim$ 2% that is centered in the middle stratosphere near 10 hPa ($\sim$ 32 km) while the response above 2 hPa is nearly zero.

The three models that do produce a significant averaged upper stratospheric response yield results shown in the top panel of Figure 1. The CESM1-WACCM response is centered at roughly 4 hPa ($\sim$ 38 km) while the MIROC-ESM-CHEM and MRI-ESM1 responses are centered at a slightly higher level of 3 hPa or $\sim$ 40 km. In all three cases, the peak amplitude averaged over all months is near 3%. Above the stratopause ($\sim$ 1 hPa), the MRI-ESM1 response is largest ($>$ 2%) at high latitudes in both hemispheres.

As also seen in Figure 1, several models (CESM1-WACCM and GISS-E2-H) produce strong and apparently significant ozone responses in the lower stratosphere ($\sim$ 50 hPa). On the other hand, MIROC-ESM-CHEM and MRI-ESM1 produce reduced and much less significant responses at this level, indicating that the modeled lower stratospheric ozone response could be sensitive to details of the model formulation. For example, the lower stratospheric response of GISS-E2-R is similar to but weaker than that of GISS-E2-H, suggesting that the coupled ocean model is a factor in producing it. In the case of CESM1-WACCM, the lower stratospheric response is more continuous with latitude but is largest in the tropics.

Because the time period considered here includes two major volcanic eruptions (El Chichòn in 1982 and Pinatubo in 1991) that followed solar maxima in 1980 and 1989, it is possible that the lower stratospheric ozone signal in some of the models of Figure 1 is affected by aliasing, i.e., lack of complete orthogonality between the solar and volcanic aerosol basis function time series (Solomon et al. 1996; Lee and Smith 2003). This is especially possible if the modeled lower stratospheric chemistry or dynamics is overly sensitive to volcanic aerosol effects (e.g., enhanced heterogeneous ozone losses or radiative heating). For example, Dhomse et al. (2011) applied the SLIMCAT chemical transport model developed at the University of Leeds (Chipperfield 1999; 2006) to show that the modeled ozone solar response in the tropical lower stratosphere is amplified by aliasing from the volcanic eruptions because the model overestimates ozone losses during high aerosol loading periods. The extent to which a similar aliasing may occur in a version of WACCM (WACCM3.5) without a coupled ocean (forced using observed sea surface temperatures and sea ice concentrations) has recently been investigated by Chiodo et al. (2014). By carrying out simulations with and without including volcanic aerosol forcing, it was found that most of the apparent solar-induced variation of tropical lower stratospheric ozone and temperature in the model is due to the two major volcanic events mentioned above. It was therefore inferred that the part of decadal variability in tropical lower stratospheric observations that can be attributed to solar variability may be smaller than previously believed. This may indeed be the case (see the next section). However, it is also possible that the modeled lower stratospheric ozone in WACCM is overly sensitive to volcanic aerosol effects, as was apparently the case for the SLIMCAT model. The results of Figure 1 suggest that this could be true since the apparent lower stratospheric solar signal is unusually large and significant in CESM1-WACCM compared to other models. In future work, this could be investigated further by (a) conducting a separate analysis for a period without powerful volcanic eruptions; and (b) repeating the MLR analysis over the 1979-2005 period with 1-2 years after the two volcanic eruptions excluded.

Figure 2 shows corresponding results for the annually averaged monthly temperature solar regression coefficients, expressed as the change in Kelvin from solar minimum to maximum (defined above). The individual ensemble mean monthly temperature solar regression coefficients are plotted in Figures S8-S13 for the 6 models. The annual mean results of Figure 2 are not very different from those shown in Paper 1, which used TSI rather than Mg II as the solar predictor and which analyzed the full suite of CMIP-5 models. Nevertheless, we show them here for completeness. As seen in the figure, the annual mean temperature results resemble the ozone results of Figure 1 since the ozone change contributes significantly to the radiative heating change from solar minimum to maximum in the stratosphere (e.g., Gray et al. 2009). The CESM1-WACCM model produces the largest temperature response in the tropical lower stratosphere (peaking near 1 K) compared to the other models and also produces a significant response exceeding 1 K above 2 hPa. The GFDL-CM3 model produces the least significant results with amplitudes of $\sim$ 0.5 K near the stratopause at most latitudes while the MRI-ESM1 model produces the strongest and most significant temperature response throughout the low-latitude stratosphere, exceeding 1 K above the 2 hPa level. The two GISS-E2 models produce a significant temperature response of intermediate amplitude ($>$ 0.5 K) at most levels in the tropical stratosphere. Finally, the MIROC-ESM-CHEM model produces a significant upper stratospheric response that is locally larger than 1 K in amplitude and has a weaker response in the lower stratosphere compared to most of the other models.

Turning to the monthly model ozone and temperature solar coefficients plotted in Figures S1-S6 and S8-S13, a seasonal evolution of the solar-induced signal is apparent. In the summer hemisphere for all models, the thermal response in the upper stratosphere tends to shift toward higher latitudes, reflecting the reduced solar-zenith angle during that season and the longer duration of daily solar heating at polar latitudes (midnight sun). However, for the models in the top panels of Figures 1 and 2 with a relatively large upper stratospheric ozone and temperature response (CESM1-WACCM, MIROC-ESM-CHEM, and MRI-ESM1), there is also a tendency for large negative latitudinal ozone and temperature gradients to develop at high latitudes in the winter hemisphere. A similar tendency for temperature averaged over all high-top models during northern winter was also shown in Figure 7 of paper 1. Averaged over all 4 of the CESM1-WACCM ensemble members, the large negative ozone and temperature gradients are mainly seen in the southern hemisphere in June and July but are also present in the northern hemisphere winter for 2 of the 4 members (not shown). In the case of the single MIROC-ESM-CHEM simulation, it occurs in December at high northern latitudes and in July/August at high southern latitudes for both ozone and temperature. The same is true for the single MRI-ESM1 simulation. For the latter two models, the negative latitudinal gradients are noticeably larger in the southern hemisphere winter.

3. Comparisons With Observational Estimates

3.1. Ozone

Continuous global satellite remote sensing measurements of stratospheric ozone have been obtained since late 1978 (WMO 2007). These measurements, like those of SSI, are subject to uncertainties including degradation with time and intercalibration offsets between different instruments. The longest continuous record of stratospheric ozone concentrations by a single instrument was obtained by the Stratospheric Aerosol and Gas Experiment (SAGE) II, beginning in November of 1984 and ending in August, 2005. The solar occultation measurement technique employed by SAGE yields a relatively good vertical resolution approaching 1 km (e.g., McCormick et al. 1989). Analyses of these data indicate substantial variations of 2 to 4% from solar minimum to maximum extending from $\sim$ 5 hPa to and above the stratopause at low latitudes (e.g., Soukharev and Hood 2006; Randel and Wu 2007; Kyrölä et al. 2013; Remsberg 2014; see Figure 3c below). However, due to the sparse sampling of the SAGE solar occultation measurements, only annual mean regression coefficients can be accurately estimated.

A second long-term data set with more complete sampling but less continuity and less vertical resolution ($\sim$ 8 km) has been constructed at the U.S. Goddard Space Flight Center by merging together vertical ozone soundings by a series of solar backscattered ultraviolet (SBUV) instruments on Nimbus 7 (late 1978 to 1990) and subsequent U.S. National Oceanic and Atmospheric Administration (NOAA) operational satellites (McPeters et al. 2013; Kramarova et al. 2013). The data obtained by the Nimbus 7 SBUV instrument were at a nearly constant local time while data acquired with SBUV/2 instruments on the NOAA satellites beginning with NOAA 11 in 1989 were more affected by orbital drifts that caused the local time of measurement to vary during many of these missions. In the upper stratosphere ($\sim$ 2 hPa and above), this can introduce artificial trends since there is a significant diurnal variation of ozone at these levels. Multiple linear regression (MLR) analyses of the merged SBUV data through 2003 yield a substantial annual mean solar cycle variation of 3 to 4% at $\sim$ 2 hPa and above in the upper stratosphere at low latitudes (Soukharev and Hood 2006; Tourpali et al. 2007). As shown in the latter references, seasonal (e.g., northern winter and summer) mean regression coefficients can also be estimated using the more densely sampled, merged SBUV data set. However, as discussed further below, the SBUV results have significant uncertainties imposed by the shortness of the data record (no more than 3.5 solar cycles) and the low vertical resolution of the individual profile measurements.

To allow a more direct comparison with the annually averaged monthly model ozone solar regression coefficients of Figure 1 and the monthly coefficients of Figures S1-S6, the analysis of Soukharev and Hood (2006) was extended to calculate monthly merged SBUV ozone regression coefficients using the same MLR model (1) that was applied to the CMIP-5 model data. Specifically, the monthly mean Version 8 merged SBUV ozone profile data set covering 1979-2003 was reanalyzed to calculate individual monthly solar regression coefficients using the updated statistical model (1), including the more conservative autocorrelation correction described in section 2 and Paper 1. The ENSO basis function in this case is the observed Niño 3.4 index and the two QBO empirical orthogonal functions are calculated from the ERA Interim reanalysis data as described in Paper 1. The N3.4 time series is lagged by 3 months to account for the observed delay in the stratospheric response to surface ENSO variability (e.g., Hood et al. 2010). The analysis is limited to the period prior to 2004 to allow direct comparisons with the results of Soukharev and Hood (2006) and Tourpali et al. (2007) and to avoid any effects of a drift in the NOAA 16 orbit, which began in early 2004.

Figure 3a shows the annually averaged SBUV monthly solar regression coefficients to allow a direct comparison to the model annually averaged coefficients of Figure 1. Specifically, Figure 3a was produced by averaging together the 12 monthly SBUV ozone solar regression coefficients and the corresponding standard deviations at each grid point. The individual monthly SBUV solar regression coefficients are plotted in Figure S14. Regression coefficients and standard deviations at a given grid point were calculated from the 25 monthly means over 1979-2003. Figure 3b shows the annual mean SBUV solar regression coefficients obtained by considering each monthly anomaly (monthly mean minus long-term monthly mean) as an independent data point ($25 \times 12 = 300$). The annual mean coefficients of Figure 3b are more statistically significant than the annually averaged monthly coefficients of Figure 3a, as would be expected from the increased number of data points. In both cases, the per cent change in ozone from solar minimum to maximum is largest in the uppermost stratosphere, especially in the tropics and at high latitudes in both hemispheres. In the tropical middle stratosphere ($\sim$ 4 hPa), the response is a minimum and is statistically insignificant. Positive responses are also obtained in the extratropical middle stratosphere and in the lower stratosphere near 50 hPa. The annually averaged monthly and annual mean ozone solar regression coefficients in Figures 3a,b are only marginally significant in the lower stratosphere. This differs from the results of Soukharev and Hood (2006) and Tourpali et al. (2007), who found apparently significant annual mean coefficients in much of the lower stratosphere. The reduced significance obtained here is probably due to the use of alternate basis functions for volcanic aerosol and the QBO, as well as to the more conservative autocorrelation correction. However, the monthly regression coefficients remain statistically significant during certain months, especially July and August as seen in Figure S14. Also, analyses of column ozone, which is dominated by lower stratospheric ozone, as a function of longitude and latitude yield significant solar regression coefficients at low latitudes during the northern summer and winter seasons (Hood and Soukharev 2012).

Comparing the annually averaged monthly SBUV ozone solar regression coefficients of Figure 3a with the corresponding model coefficients of Figure 1, none of the models appears to yield an ozone response that agrees to first order with that derived from the SBUV observations. None of the models produces a relative minimum in the tropical response near 4 hPa, although CESM1-WACCM produces a tropical minimum near the 20 hPa level. The averaged monthly SBUV coefficients yield maxima near the stratopause exceeding 6% in the tropics, decreasing to $\sim$ 4% at middle latitudes, and increasing again to more than 6% at high latitudes. None of the models produces a response that maximizes near the tropical stratopause with reductions at midlatitudes. The 3 models in the top panel of Figure 1 do produce relatively large ($>$ 2%) ozone responses in the upper stratosphere but they are centered near 4, 3, and 3 hPa, respectively, while the SBUV response is centered above 1 hPa. The 3 models in the bottom panel of Figure 1 produce responses at even lower levels (centered at or below the 10 hPa level).

However, some of the disagreements between Figure 3a and Figure 1 may be a consequence of measurement uncertainties. Although the merged SBUV data set is the only available record with sufficient sampling and length to allow reasonable estimation of seasonally resolved ozone solar regression coefficients, there could be an artificial bias in these data toward higher altitudes. Evidence that this may be the case comes from a consideration of the annual mean solar regression coefficients obtained from SAGE data, which have much better vertical resolution ($\sim$ 1 km vs. $\sim$ 8 km for SBUV). Figure 3c shows the result of an analysis of Version 6 SAGE II data (updated from Soukharev and Hood 2006) using the improved MLR model (1) and autocorrelation correction. In agreement with previous analyses (e.g., Randel and Wu 2007), the region of minimum tropical response based on SAGE data is centered near 10 hPa ($\sim$ 31 km) while that of Figure 3b based on SBUV data is centered near 4 hPa ($\sim$ 38 km). The SAGE-derived ozone solar regression coefficients exceed 2% and are statistically significant at all levels above 5 hPa ($\sim$ 36 km) continuing up to at least 0.5 hPa ($\sim$ 54 km). On the other hand, the annual mean SBUV coefficients of Figure 3b exceed 2% in the tropics only at levels above 2 hPa ($\sim$ 42 km).

Independent evidence that the ozone 11-year solar regression coefficients derived from merged SBUV data are underestimated at levels below 2 hPa in the tropics has also been presented by Fioletov (2009). He predicted 11-year ozone variations at low latitudes using the observed ozone response to short-term solar rotational ($\sim$ 27-day) UV variations and then compared these projected variations to observed decadal variations in data from the individual SBUV instruments. It was found (see his Figure 12) that the projected variation remained significant down to altitudes as low as 33 km even though no response was detectable in the combined SBUV time series. Also, the SBUV data from the Nimbus 7 time period (1979-1990) contained an anomalously large 11-year variation at altitudes above 44 km compared to the projected variation and to that recorded during later solar cycles.

Accepting the possibility that the actual observed ozone response extends downward to at least the 5 hPa level in the tropics, the three modeled ozone responses in the top panel of Figure 1 compare more favorably with the observations. To illustrate this, Figure 4 plots tropical (25°S to 25°N) area-weighted averages of the SAGE II results from Figure 3c at a series of pressure levels up to 1 hPa ($\sim$ 48 km) together with corresponding averages of the model results of Figure 1. As seen in Figure 4a, the three models in the top panel of Figure 1 yield ozone response profiles that fall well within the 2σ error bars of the tropical mean SAGE II solar coefficients. As seen in Figure 4b, the remaining models produce tropical mean upper stratospheric ozone responses that are outside of the 2σ error bars at altitudes above 40 km. Also, the altitude dependence of the solar ozone response for the latter models differs noticeably from that estimated from the SAGE II data.

3.2. Temperature

Continuous global satellite remote sensing measurements of atmospheric temperature also began in the late 1970's. In Paper 1, model temperature solar responses were compared to estimates derived from the three most recent reanalysis meteorological data sets, MERRA, ERA-Interim, and JRA-55 (Mitchell et al. 2014b, in review). As discussed in Paper 1, a maximum solar-induced temperature response in the reanalyses of several Kelvin is obtained at low latitudes well above the stratopause ($\sim$ 0.5 hPa), whereas the maximum expected theoretical response is about half this amplitude and is centered near the stratopause (Gray et al. 2009). It was therefore suggested that increased errors in the reanalyses at levels above 1 hPa where data assimilation is poorly constrained by observations may be responsible for the unexpectedly large apparent solar signal. A comparison of direct satellite Stratospheric Sounding Unit (SSU) measurements with reanalysis temperature time series supported this inference (Mitchell et al. 2014b, in review).

Here, we consider specifically temperature and zonal wind data from one of the reanalyses, ERA Interim (Dee et al. 2011), which are publicly available to a level of 1 hPa (http://apps.ecmwf.int/datasets). As described in the Appendix, at least one source of errors in this data set, step changes in upper stratospheric temperature occurring near the times of major changes in instrumentation or processing of assimilated data, can be empirically minimized to produce an "adjusted" ERA Interim zonal mean temperature data set. Such an empirical minimization procedure is not generally applicable to other reanalyses (e.g., MERRA) because step changes were usually replaced with ramp functions in the archived data sets.

Figure 5a shows the annually averaged monthly solar temperature regression coefficient derived from the adjusted ERA data over the 1979-2012 period, expressed as the change in Kelvin from solar minimum to maximum as defined in section 2.4. The entire available 34-year record is considered rather than only the 1979-2005 period because the results change only slightly as compared to the shorter record and the statistical significance is improved. The individual monthly ERA Interim solar temperature regression coefficients are plotted in Figure S15. Figure 5b shows the corresponding annual mean coefficient obtained when all available data points ($12 \times 34 = 408$) are analyzed. The annual mean tropical upper stratospheric response is larger in peak amplitude ($\geq$ 1.5 K) and is formally significant while the annually averaged monthly response of Figure 5a has a peak amplitude of $\geq$ 1 K and is only marginally significant. Overall, Figure 5b agrees well with previous studies, which analyzed the ERA-40 reanalysis data set through 2001 or extensions thereof (e.g., Crooks and Gray 2005; Frame and Gray 2010). It also agrees well with an alternate analysis of ERA Interim data by Mitchell et al. (2014b, in review). As shown in their Figure 7, the peak response in the tropics occurs near 2 hPa and the high-latitude maxima at 1 hPa in Figure 5b extend up to 0.3 hPa ($\sim$ 55 km).

Comparing the annual ERA temperature results of Figure 5 with the annual observational ozone results of Figure 3, several similarities are notable. First, in the tropics, the ozone response is largest in the upper stratosphere (down to $\sim$ 2 hPa for SBUV and down to $\sim$ 5 hPa for SAGE) while the temperature response is also largest in the tropical upper stratosphere (1 to 3 hPa). Second, at high latitudes near the 1 hPa level, the temperature response maxima of order 2 K compare favorably with the SBUV ozone response maxima of order 5-6%. A comparison of the monthly ERA temperature results of Figure S15 with the corresponding SBUV ozone results of Figure S14 shows that the high-latitude responses of both ozone and temperature occur in the summer hemisphere. They are therefore presumably a consequence of the enhanced photolytic and radiative effects of more continuous solar radiation at reduced solar-zenith angles in the polar regions during the summer season. Third, the lower stratospheric subtropical temperature response maxima agree qualitatively with responses seen in the SBUV data at comparable pressure levels, especially when the individual monthly responses are examined. Specifically, as seen in Figure 3a for the annually averaged SBUV monthly coefficients, marginally significant ozone response maxima of order 3% are present in the subtropical lower stratosphere near 50 hPa. These coefficients are formally significant with larger amplitudes (up to 8%) during July and August (Figure S14). Similarly, the ERA Interim monthly coefficients are formally significant with amplitudes $>$ 0.5 K near 50 hPa only during June, July, and August (Figure S15).

Comparing the annual temperature responses of Figure 5 with the corresponding model responses of Figure 2, it is first apparent that the three models in the top panel of Figure 2 yield statistically significant minimum-to-maximum temperature changes in the tropical upper stratosphere that are closer in magnitude ($>$ 1 K) to those obtained from the adjusted ERA data. This is further shown in Figure 6, which compares tropical averages of the ERA Interim temperature solar regression coefficients to similar averages of the model solar coefficients, analogous to the tropical ozone comparison in Figure 4. None of the models, however, produces secondary temperature response maxima at high polar latitudes that are similar to those obtained in the ERA Interim data. The observationally estimated maxima are likely to be real because they are seen in both hemispheres in summer and correspond to similar polar ozone maxima found in SBUV data. An examination of Figures S8-S13 shows that most of the models (except GFDL-CM3) produce broad maxima in the temperature response at high summer latitudes near the stratopause but the amplitudes are in the range of 1.0-1.5 K, which is less than obtained from the reanalysis data.

As also seen in Figures 2 and 6, most of the models (4 of 6) produce broad positive responses in the tropical lower stratosphere ($\sim$ 50 hPa) that are statistically significant. One of these, CESM1-WACCM, produces localized subtropical response maxima that are qualitatively similar to those obtained from the ERA Interim data. However, the peak amplitudes in the lower stratosphere for CESM1-WACCM ($\sim$ 1 K) are nearly a factor of two larger than those in Figure 5b ($\sim$ 0.6 K). Also, as seen in Figure S8, the monthly model temperature responses in this location are significant during most months while, as seen in Figure S15, the corresponding observational monthly temperature responses near 50 hPa are significant only during NH summer. As seen in Figure S1, the CESM1-WACCM 11-year ozone response in the lower stratosphere is large and significant during nearly all months while, as seen in Figure S14, the observationally estimated tropical ozone response near 50 hPa is significant only during NH summer. As discussed in section 2.4, at least part of the lower stratospheric 11-year ozone response in this model may be due to aliasing from the two major volcanic eruptions during 1979-2005 if the model ozone chemistry is overly sensitive to volcanic aerosol effects. Consistently, as shown in Figure 4 of Paper 1, use of a longer time series (1850-2005) to reduce cross-correlation between the predictors results in a weaker lower stratospheric response for both high-top and low-top models. Hence, it is unclear whether the CESM1-WACCM CMIP-5 simulations can provide useful constraints on the origin of the solar-induced lower stratospheric ozone and temperature responses that are derived from observations over the 1979-2005 time period. It would be straightforward to investigate this further in future work, as discussed in section 2.4.

3.3. Zonal Wind

The apparent offset errors found in ERA Interim temperature data in the upper stratosphere should be less problematic for the derived zonal wind field since the latter depends primarily on latitudinal temperature gradients, which are less sensitive to sudden steps in mean temperatures. The MLR model (1) was therefore applied to the ERA Interim zonal wind data over 1979-2012 to obtain the monthly solar regression coefficients plotted in Figure S16. Again, we consider the extended time period because the results are very similar to those obtained for 1979-2005 and the statistical significance is slightly increased. The regression coefficients are expressed as the change in the zonal wind in meters/second from solar minimum to maximum, as defined in section 2.4.

As seen in Figure S16, the ERA Interim zonal wind solar regression coefficients are only marginally significant during most months but are characterized by a consistent dependence on season in both hemispheres. Specifically, the largest zonal wind changes from solar minimum to maximum are estimated to occur at northern and southern midlatitudes in the uppermost stratosphere during the winter season of each hemisphere. During northern winter, the largest zonal wind response (up to 9 m/s) is obtained during November and December while, during southern winter, the largest response (up to 15 m/s) is obtained during July and August. During some of these months (December, July, and August), the positive zonal wind response at subtropical to middle latitudes is complemented by a weaker negative response at higher latitudes. These results are similar to those obtained previously by Frame and Gray (2010) using ERA 40 reanalysis data and operational analyses for the 1979-2008 period (see their Figure 7). The existence of 11-year wintertime zonal wind anomalies in the midlatitude upper stratosphere was first reported based on rocketsonde data by Kodera and Yamazaki (1990). Later investigations of stratospheric data compiled by the former U.S. National Meteorological Center found evidence for a similar dynamical response in the southern winter (Hood et al. 1993). The existence of an upper stratospheric zonal wind response to solar forcing during early winter is a basic element of the top-down mechanism for solar induced regional climate change (Kodera and Kuroda 2002; Matthes et al. 2006).

Because the observationally estimated zonal wind response is a maximum during NH early winter (November and December) and SH middle winter (July and August), Figure 7 shows the mean ozone, temperature, and zonal wind responses for these particular time periods. This figure is intended to illustrate the basic seasonal dependence of the observed solar signal in the stratosphere. The wintertime positive zonal wind responses in both hemispheres are accompanied by strong negative latitudinal gradients in the ozone and temperature responses that are centered approximately on the latitude of the zonal wind response.

3.4. Seasonal Model Comparisons

Finally, we wish to compare in more detail the seasonal ozone, temperature, and zonal wind responses obtained from the 6 high-top CMIP-5 models with interactive chemistry (Table I) to the observationally estimated responses of Figure 7. The main objective is to determine whether the 3 models in the top panels of Figures 1, 2, 4, and 6 that produce substantial upper stratospheric ozone and temperature responses also produce a seasonally dependent response of ozone, temperature, and zonal wind that compares favorably with observations. A second objective is to identify any specific model simulations that yield the best agreement with the observations. For this purpose, the monthly solar regression results for zonal wind for each of the 6 interactive models of Table I are plotted in Figures S17-S22.

Prior to considering the 6 interactive models of Table I, it is useful to consider an ensemble of 3 simulations performed by a high-top model without interactive chemistry (MIROC-ESM). This model is a version of MIROC-ESM-CHEM but without the interactive chemistry module. It differs from other high-top CMIP-5 models without interactive chemistry in that the ozone variation that was prescribed for this model did not include a representation of the solar cycle (Watanabe et al. 2011). Like the other CMIP-5 models, this model did however impose a solar cycle variation of SSI (the NRL SSI). The model temperature and zonal wind responses therefore provide an interesting test of whether a realistic 11-year ozone variation in the upper stratosphere is necessary for producing a realistic thermal and dynamical response in winter. Figure 8 shows the ozone, temperature, and zonal wind changes from solar minimum to maximum during early northern winter and middle southern winter in the same format as Figure 7. (These averages were calculated from the ensemble mean monthly temperature and zonal wind solar regression coefficients plotted in Figures S23 and S24.) It is evident that this model produces no significant solar-induced latitudinal gradient in the temperature response and no corresponding positive zonal wind anomalies similar to those seen in Figure 7 even though a solar cycle SSI variation (but no accompanying ozone variation) was imposed. It is also interesting to note that there is no significant 11-year response of lower stratospheric temperature in either this model or MIROC-ESM-CHEM (Figure 2b) caused by aliasing from the two major volcanic eruptions during 1979-2005. Apparently, the volcanic aerosol effects on ozone chemistry, radiative heating, and dynamics in this model are reduced in comparison to those for some other models (e.g., CESM1-WACCM) so that little or no aliasing occurred.

Next, consider the 3 interactive models of Table I that did not produce a substantial upper stratospheric ozone response and produced a relatively weak upper stratospheric temperature response (GFDL-CM3, GISS-E2-H, and GISS-E2-R). Averaging together the ensemble and zonal mean ozone, temperature, and zonal wind responses during November-December and July-August for these 3 models yields the mean responses shown in Figure 9. Again, no significant latitudinal temperature response gradients and no significant zonal wind anomalies are produced by these models.

Next, consider the 3 interactive models of Table I that did produce a substantial upper stratospheric ozone and temperature response (CESM1-WACCM, MIROC-ESM-CHEM, and MRI-ESM1). Averaging together the ensemble and zonal mean ozone, temperature, and zonal wind responses during the same time periods for these 3 models yields the mean responses shown in Figure 10. For these models, a mean negative latitudinal ozone gradient is obtained centered on latitudes of $\sim 70°$N in November-December and $70°$S in July-August. Accompanying temperature gradients with zero lines centered on about $60°$ in both hemispheres are obtained. Corresponding positive zonal wind anomalies with amplitudes of $\sim$ 3 m/s in November-December centered at $\sim 60°$N and $\sim$ 8 m/s in July-August centered near $45°$S are obtained, although only the southern hemisphere one is marginally significant. The structure of the southern hemisphere wind signal is similar to that estimated from observations in that a weaker negative wind anomaly is present at higher latitudes. However, the mean amplitudes in both hemispheres are weaker by at least a factor of two than those estimated from the ERA Interim data in Figure 7.

Lastly, Figure 11 shows a similar plot for the interactive model that produced the strongest and most significant 11-year response of upper stratospheric ozone, the MRI-ESM1 model (Figures 1c and 2c). Only one historical simulation was completed for this model so there is no guarantee that the results are representative of those for an ensemble mean. Nevertheless, we show them to illustrate that a larger response in the northern hemisphere is possible in at least some simulations. As seen in the figure, the upper stratospheric zonal wind anomaly is marginally significant with an amplitude of $\sim$ 6 m/s and is centered near $50°$N close to the stratopause. For comparison, the corresponding observational zonal wind anomaly has an amplitude of $\sim$ 7 m/s and is centered near $30°$N (Figure 5c). The model positive zonal wind anomaly in the southern hemisphere in July-August is formally significant with a peak amplitude of 8 m/s near 2 hPa, which compares to a marginally significant anomaly derived from the ERA data with a peak amplitude of $\sim$ 13 m/s near the stratopause.

4. Summary and Discussion

A prerequisite for a successful model simulation of the top-down component of solar-induced climate change is that the model should produce an upper stratospheric response of ozone, temperature, and zonal wind to 11-year solar forcing that agrees at least to first order with available observations (Kodera and Kuroda 2002; Matthes et al. 2006; Yukimoto and Kodera 2007; Hood et al. 2013). Since continuous global satellite measurements of stratospheric ozone and temperature began in 1979 and since the CMIP-5 model simulations cover the period up to 2005, this study has focused on the 1979-2005 period for detailed comparisons of solar signals in CMIP-5 models with available observations. Only the 6 models with high tops and interactive ozone chemistry were considered (Table I). The Mg II solar UV index, derived from satellite SSI data, was adopted as the solar predictor or basis function in the MLR analysis (rather than TSI as done in Paper 1) because it is available for this particular time period and produces larger and more statistically significant solar regression coefficients in stratospheric ozone data (e.g., Figure S7).

In section 2.4, it was found that three of the six models in Table I (CESM1-WACCM, MIROC-ESM-CHEM, and MRI-ESM1) produce substantial solar-induced responses of ozone and temperature in the upper stratosphere (Figures 1 and 2). This result was based on MLR analyses over 1979-2005 of 4 ensemble members for CESM1-WACCM, 1 member each for MIROC-ESM-CHEM and MRI-ESM1, and 5 members each for GFDL-CM3, GISS-E2-H, and GISS-E2-R. As found in sections 3.1 and 3.2, the observationally estimated annually averaged monthly ozone and temperature solar regression coefficients for the period after 1979 (Figures 3 to 6) compare favorably with the corresponding coefficients for CESM1-WACCM, MIROC-ESM-CHEM, and MRI-ESM1 in the upper stratosphere, especially when uncertainties in the observational estimates are taken into account. The remaining three models (GFDL-CM3, GISS-E2-H, and GISS-E2-R) yield much weaker upper stratospheric responses that are difficult to reconcile with available observations. However, the latter three models do, in effect, provide a valuable baseline or set of control runs against which results for the three models with a substantial upper stratospheric response can be compared.

As discussed in section 2.2, there are some significant differences in the radiation and photolysis codes for the six models that could potentially explain why only three of the models produce substantial 11-year upper stratospheric ozone variations that agree with observational estimates. In the case of the GFDL-CM3 model, which produced the weakest 11-year ozone variation at most altitudes in the stratosphere, the applied photolysis rate calculation scheme appears to have been designed mainly for tropospheric applications and could therefore have omitted O_2 photolysis. In the case of the two GISS-E2 models, the weak 11-year upper stratospheric ozone variation could potentially be caused by omissions of O_2 absorption in the radiation code and the SRB contribution to O_2 dissociation in the photolysis rate code. The three models with substantial upper stratospheric ozone variations have fewer issues overall, although WACCM also omits O_2 absorption below 65 km and MIROC-ESM-CHEM omits water vapor photolysis. These deficiencies could potentially lead to some overestimation of the upper stratospheric ozone response. The MRI-ESM1 model has no obvious omissions that would affect the solar-induced ozone variation in the upper stratosphere.

As found in section 3.3, in agreement with previous studies, the observationally estimated zonal wind response to 11-year solar forcing, although only marginally significant, is a maximum during NH early winter (November and December) and during SH middle winter (July and August). These zonal wind anomalies are accompanied by negative latitudinal gradients in the ozone and temperature responses during the same months in both winter hemispheres (Figure 7). Therefore, in section 3.4, a more detailed comparison of the ozone, temperature, and zonal wind responses from the 6 selected high-top models with the observationally estimated responses was carried out. It was first found (Figure 8) that three simulations using a version of MIROC-ESM-CHEM with no interactive chemistry and no representation of the solar cycle in its prescribed ozone variation produce no significant negative latitudinal temperature gradients or positive zonal wind anomalies in either winter hemisphere, even though a solar cycle variation of SSI (the NRL SSI model) was imposed in the model. This shows that such a model with no significant 11-year stratospheric ozone variation and a conservative SSI variation is not able to produce a realistic upper stratospheric seasonal response. The three interactive chemistry models that did not produce a significant annually averaged response of upper stratospheric ozone and only a weak temperature response also yielded no significant seasonal response in either hemisphere (Figure 9). The three interactive models that did produce annually averaged ozone and upper stratospheric responses agreeing to first order with observational constraints yielded a stronger combined upper stratospheric seasonal response in both hemispheres, especially in the southern hemisphere in July and August (Figure 10). The multi-model mean zonal wind response for these three models in November and December has an amplitude of only 3 m/s and is not statistically significant. But some simulations using these three models do produce a relatively strong zonal wind response during northern early winter that is consistent with observational estimates. In particular, the single MRI-ESM1 model simulation produces a mean zonal wind anomaly of $\sim$ 8 m/s during November and December (Figure 11). Several of the CESM1-WACCM simulations also produced a large positive wind anomaly during this season, although the ensemble mean amplitude was much less. Further simulations using the MRI-ESM1 model are needed to test whether the stronger northern winter zonal wind anomalies are a robust feature of this model for a conservative SSI variation.

The model ozone and temperature response gradients and the corresponding zonal wind anomalies of Figures 10 and 11 occur at somewhat higher latitudes than those that are estimated from observations (Figure 7). This difference has also been noted previously by Kodera et al. (2003) and may be related to an overall tendency for general circulation models to simulate a polar night jet that is centered at a higher latitude than is observed. For example, the climatological polar night jet at the stratopause ($\sim$ 1 hPa) calculated from the ERA Interim data in December is centered at a latitude between 45° and 50° N. In contrast, most GCMs produce a night jet during this month that is centered near 60° N. Kodera et al. (2003) have also argued that the inability of GCMs to produce an amplitude of the solar-induced polar night jet oscillation that is as large as estimated from observations is related to a failure to realistically produce interannual variability in the polar night jet amplitude.

The negative latitudinal ozone response gradients in the winter high-latitude upper stratosphere that are found in both observations (Figure 7) and model simulations (e.g., Figures 10, 11, S2k) are too strong to be due to the decrease with increasing latitude of the solar UV-induced ozone production rate. Instead, they are probably dynamical in origin since they are associated with positive zonal wind anomalies. It is unlikely that direct dynamical transport of ozone itself plays a role because the ozone chemical lifetime in the upper stratosphere is much shorter than dynamical timescales. Rather it is more likely that ozone is responding photochemically to dynamically induced changes in temperature and/or other minor species concentrations that affect the ozone balance. The temperature changes seen in both observations and models have the same sign as the ozone changes, which is inconsistent with temperature feedback effects on ozone photochemistry (temperature increases alone result in ozone decreases, and vice versa in the upper stratosphere). Therefore, dynamically induced changes in minor species concentrations that are important for ozone catalytic losses may be implicated. For example, odd nitrogen has a photochemical lifetime near the stratopause ($\sim$ 1 month) that is much longer than dynamical timescales (e.g., Brasseur and Solomon 2005). Hence, a transport-induced increase in the latitudinal gradient of odd nitrogen in the upper stratosphere under solar maximum conditions would contribute to the negative latitudinal gradient in the ozone response for both models and observations. More detailed diagnostic analysis of the CMIP-5 model data is needed to test whether this process or others are involved.

Regardless of the exact origin of the negative latitudinal ozone response gradients, it is clear that they would assist in amplifying the zonal wind response. A strong negative latitudinal ozone gradient will radiatively enhance the negative latitudinal temperature gradient, which, by thermal wind balance, would amplify the zonal wind anomaly. This could therefore represent a positive feedback mechanism for producing a stronger upper stratospheric dynamical response than expected for models that impose a conservative 11-year SSI variation. In any case, the results of Figures 1, 2, 4, 6, 8, 9, 10, and 11 support the view that models with high tops, interactive ozone chemistry, and a capability to simulate substantial ozone responses in the upper stratosphere are better able to produce a strong upper stratospheric dynamical response. Such a dynamical response can, in turn, lead to significant troposphere-ocean signals in coupled models via the top-down mechanism (e.g., Yukimoto and Kodera 2007).

Acknowledgements

The work reported here was directly motivated by the SPARC SOLARIS-HEPPA SolarMIP project. The authors thank all CMIP-5 modeling groups responsible for producing the simulations summarized in Table I and for providing their model data to the CMIP-5 archive. Special thanks to Makato Deushi and Kiyotaka Shibata for clarifying the nature of the chemistry component of the MRI-ESM1 model and to Dan Marsh for helpful comments about the WACCM model. Work at the University of Arizona was supported by grant 1251092 from the U.S. National Science Foundation and by grant NNX14AD44G from NASA. Work at the University of Thessaloniki was supported by European Cooperation in Science and Technology (COST) Action ES1005 (Towards a more complete assessment of the impact of solar variability on the Earth's Climate - TOSCA). Work at the University of Oxford was supported by the U.K. Natural Environment Research Council as well as by TOSCA. Work at the World Radiation Center was supported by the Swiss National Science Foundation under grant CRSII2-147659 (FUPSOL II) and by the State Secretariat for Education, Research and Innovation of the Swiss Confederation under grant C11.01124 (SOVAC). Work at the GEOMAR Helmholtz Centre for Ocean Research in Kiel, Germany is partly supported within the Helmholtz-University Young Investigators Group NATHAN funded by the Helmholtz Association through the President's Initiative and Networking Fund and by the GEOMAR.

Appendix

In this appendix, evidence for artificial offsets (step changes) in zonally averaged ERA Interim temperature data in the upper stratosphere (5 hPa and above) is discussed and an empirical procedure is applied to adjust the data to minimize the offsets. The data were obtained at levels ranging from 1000 to 1 hPa (the highest level available for public access) from the European Centre for Medium-Range Weather Forecasts (http://apps.ecmwf.int/datasets).

The top panel of Figure A1 compares deseasonalized anomalies (deviations from the long-term monthly means) of ERA Interim temperature data at the highest available level (1 hPa) averaged over low latitudes (35°S to 35°N) to the Mg II solar UV index over the 1979-2012 period. Large offsets occur at several points in the time series that apparently are related to major changes in satellite instrumentation and/or changes in the reanalysis procedure. The largest single offset between July and August of 1998 closely follows the launch of the first Advanced Microwave Sounding Unit (AMSU) on the NOAA 15 satellite in May of that year. The AMSU was an improvement over the Microwave Sounding Unit (MSU), which began observations together with the SSU on TIROS-N in 1978. Other smaller offsets appear to occur between June and July of 1979 and between February and April of 1985. Offset errors of this type are clearly found in the data only at the 1, 2, and 5 hPa levels.

In order to estimate the magnitude of offset errors such as those in the top panel of Figure A1, a simple average of the low-latitude temperature anomalies was calculated in a 12-month window on either side of the offsets (except for the 1979 offset for which only 6 months were available to calculate the first average). The offset errors estimated from the differences between these two averages are: 1 hPa: 1979: -4.33 K; 1985: -1.87 K; 1998: +4.94 K; 2 hPa: 1979: -3.16 K; 1985: -1.38 K; 1998: +2.25 K; 5 hPa: 1998: -2.14 K. Assuming that the offset errors estimated at low latitudes apply approximately to all latitudes, an adjusted monthly ERA Interim data set was constructed in which these estimated errors were minimized. The bottom panel of Figure A1 compares low-latitude temperature anomalies calculated from the adjusted data at 1 hPa to the Mg II UV index. As can be seen, the adjusted anomalies at this level exhibit a quasi-decadal variation that is roughly in phase with the solar cycle.

To test to what extent the offset errors may influence solar temperature regression coefficients derived from the ERA Interim data, the MLR model (1) was applied separately to the unadjusted and adjusted data. It was found that the overall spatial structure of the solar regression coefficients was surprisingly similar for the two data sets, apparently due to the ability of the MLR method to identify solar-correlated decadal variations between the offset locations. However, the amplitudes of the solar temperature regression coefficients near the stratopause are increased by about 50% when using the unadjusted data set rather than the adjusted data set. Most of this increase is due to the fact that the large positive offset error in 1998 near 1 hPa occurs during a rising phase of the solar cycle as seen in the top panel of Figure A1. Hence, the adjusted data provide a better estimate for the true amplitude of the solar-induced temperature response near the stratopause.

References

Adachi Y, Yukimoto S, Deushi M, Obata A, Nakano H, Tanaka T, Hosaka M, Sakami T, Yoshimura H, Hirabara M et al. 2013. Basic performance of a new Earth system model of the Meteorological Research Institute (MRI-ESM1). *Papers in Meteorology and Geophysics* **64**: 1-19, doi:310.2467/mripapers.64.1.

Anderson J, Balaji V, Broccoli J, Cooke WF, Delworth TL, Dixon K, Donner L, Dunne K, Freidenreich SM, Garner S et al. 2004. The new GFDL global atmosphere and land model AM2-LM2: Evaluation with prescribed SST simulations. *Journal of Climate* **17**: 4641-4673.

Austin J, Tourpali K, Rozanov E, Akiyoshi H, Bekki S, Bodeker G, Brühl C, Butchart N, Chipperfield M, Deushi M et al. 2008. Coupled chemistry climate model simulations of the solar cycle in ozone and temperature. *Journal of Geophysical Research Atmospheres* **113**: D11306, doi:10.1029/2007JD009391.

Bian H, Prather M. 2002. Fast-J2: Accurate simulations of photolysis in global climate models. *Journal of Atmospheric Chemistry* **41**: 281-296.

Brasseur GP, Solomon S. 2005. *Aeronomy of the Middle Atmosphere*. Springer.

Briegleb B. 1992. Delta-Eddington approximation for solar radiation in the NCAR Community Climate Model. *Journal of Geophysical Research Atmospheres* **97**: 7603-7612.

Chiodo G, Marsh DR, Garcia-Herrera R, Calvo N, Garcia JA. 2014. On the detection of the solar signal in the tropical stratosphere. *Atmospheric Chemistry and Physics* **14**: 5251-5269.

Chipperfield MP. 1999. Multiannual simulations with a three-dimensional chemical transport model. *J. Geophys. Res.* **104**: 1781-1805.

Chipperfield MP. 2006. New version of the TOMCAT/SLIMCAT offline chemical transport model: Intercomparison of stratospheric tracer experiments. *Quarterly Journal of the Royal Meteorological Society* **132**: 1179-1203.

Cochrane D, Orcutt DH. 1949. Application of least squares regression to relationships containing autocorrelated error terms. *Journal of the American Statistical Association.* **44**: 32-61.

Crooks SA, Gray LJ. 2005. Characterization of the 11-Year solar signal using a multiple regression analysis of the ERA-40 dataset. *Journal of Climate* **18**: 996-1015.

Dee DP, Uppala SM, Simmons AJ, Berrisford P, Poli P, Kobayashi S, Andrae U, Balmaseda MA, Balsamo G, Bauer P, et al. 2011. The ERA-Interim reanalysis: Configuration and performance of the data assimilation system. *Quarterly Journal of the Royal Meteorological Society* **137**: 553-597.

Deushi M, Shibata K. 2011. Development of an MRI Chemistry-Climate Model ver. 2 for the study of tropospheric and stratospheric chemistry. *Papers in Meteorology and Geophysics* **62**: 1-46.

Dhomse S., Chipperfield MP, Feng W, Haigh JD. 2011. Solar response in tropical stratospheric ozone: a 3-D chemical transport model study using ERA reanalyses. *Atmospheric Chemistry and Physics* **11**: 12773-12786.

Donner LJ, Wyman BL, Hemler RS, Horowitz LW, Ming Y, Zhao M, Golaz J-C, Ginoux P, Lin S-J, Schwarzkopf MD et al. 2011. The dynamical core, physical parameterizations, and basic simulation characteristics of the atmospheric component AM3 of the GFDL global coupled model CM3. *Journal of Climate* **24**: 3484-3519.

Ermolli I, Matthes K, Dudok de Wit T, Krivova NA, Tourpali K, Weber M, Unruh YC, Gray LJ, Langematz U, Pilewskie P et al. 2013. *Atmospheric Chemistry and Physics* **13**: 3945-3977.

Eyring V, Arblaster J, Cionni I, Sedlácek J, Perlwitz J, Young PJ, Bekki S, Bergmann D, Cameron-Smith P, Collins WJ et al. 2013. Long-term ozone changes and associated climate impacts in CMIP5 simulations. *Journal of Geophysical Research Atmospheres* **118**: 5029-5060, doi:10.1002/jgrd.50316.

Fioletov VE. 2009. Estimating the 27-day and 11-year solar cycle variations in tropical upper stratospheric ozone. *Journal of Geophysical Research* **114**: D02302, doi:10.1029/2008JD010499.

Frame THA, Gray LJ. 2010. The 11-yr solar cycle in ERA-40 data: An update to 2008. *Journal of Climate* **23**: 2213-2222.

Friedenreich S, Ramaswamy V. 1999. A new multiple-band solar radiative parameterization for general circulation models. *Journal of Geophysical Research Atmospheres* **104**: 31389-31409.

Garny H, Bodeker GE, Dameris M. 2007. Trends and variability in stratospheric mixing: 1979-2005. *Atmospheric Chemistry and Physics*. **7**: 5611-5624.

Gray LJ, Rumbold ST, Shine KP. 2009. Stratospheric temperature and radiative forcing response to 11-year solar cycle changes in irradiance and ozone. *Journal of the Atmospheric Sciences* **66**: 2402-2417.

Gray LJ, Beer J, Geller M, Haigh J, Lockwood M, Matthes K, Cubasch U, Fleitmann D, Harrison G, Hood L et al. 2010. Solar influences on climate. *Reviews of Geophysics* **48**: RG4001, doi:10.1029/2009RG000282.

Haigh JD. 2003. The effects of solar variability on the Earth's climate. *Philosophical Transactions: Mathematical, Physical and Engineering Sciences* **361**: 95-111.

Harder JW, Fontenla JM, Pilewski P, Richard EC, Woods TN. 2009. Trends in solar spectral irradiance variability in the visible and infrared. *Geophysical Research Letters* **36**: L07801, doi:10.1029/2008GL036797.

Heath D, Schlesinger B. 1986. The Mg 280 nm doublet as a monitor of changes in solar ultraviolet irradiance. *Journal of Geophysical Research* **91**: 8672-8682.

Hood LL. 1986. Coupled stratospheric ozone and temperature responses to short-term changes in solar ultraviolet flux: An analysis of Nimbus 7 SBUV and SAMS data. *Journal of Geophysical Research* **91**: 5264-5276.

Hood LL, Huang Z, Bougher SW. 1991. Mesospheric effects of solar ultraviolet variations: Further analysis of SME IR ozone and Nimbus 7 SAMS temperature data. *Journal of Geophysical Research* **96**: 12989-13002.

Hood LL, Jirikowic J, McCormack JP, 1993. Quasi-decadal variability of the stratosphere: Influence of long-term solar ultraviolet variations. *Journal of the Atmospheric Sciences* **50**: 3941-3958.

Hood LL, Soukharev BE, McCormack JP. 2010. Decadal variability of the tropical stratosphere: Secondary influence of the El Niño-Southern Oscillation. *Journal of Geophysical Research Atmospheres* **115**: D11113, doi:10.1029/2009JD012291.

Hood LL, Soukharev BE. 2012. The lower-stratospheric response to 11-yr solar forcing: Coupling to the troposphere-ocean response. *Journal of the Atmospheric Sciences* **69**: 1841-1864.

Hood LL, Schimanke S, Spangehl T, Bal S, Cubasch U. 2013. The surface climate response to 11-yr solar forcing during northern winter: Observational analyses and comparisons with GCM simulations. *Journal of Climate* **26**: 7489-7506.

Huang T, Walters S, Brasseur G, Hauglustaine D, Wu W, Chabrillat S, Xuexi T, Granier C, Smith A, Kockarts G. 1998. Description of SOCRATES- a chemical dynamical radiative two-dimensional model. NCAR Technical Note NCAR/TN-440+EDD, doi:10.5065/D6K0726C.

Keating GM, Nicholson III JY, Young DF, Brasseur G, De Rudder A. 1987. Response of middle atmosphere to short-term solar ultraviolet variations, 1, Observations. *Journal of Geophysical Research* **92**: 889-902.

Kodera K, Kuroda Y. 2002. Dynamical response to the solar cycle: Winter stratopause and lower stratosphere. *Journal of Geophysical Research: Atmospheres* **107**: 4749, doi:10.1029/2002JD002224.

Kodera K, Matthes K, Shibata K, Langematz U, Kuroda Y. 2003. Solar impact on the lower mesospheric subtropical jet: A comparative study with general circulation model simulations. *Geophysical Research Letters* **30**: 1315, doi:10.1029/2002GL016124.

Kodera K, Yamazaki K. 1990. Long-term variation of upper stratospheric circulation in the Northern Hemisphere in December. *Journal of the Meteorological Society of Japan* **68**: 101-105.

Kopp G, Rottman G, Rottman G. 2005. The total irradiance monitor (tim): science results: In: *The Solar Radiation and Climate Experiment (SORCE)*, Springer, pp. 129-139.

Koppers G, Murtagh D. 1996. Model studies of the influence of O_2 photodissociation parameterisation in the Schumann-Runge bands on ozone related photolysis in the upper atmosphere. *Annales Geophysicae* **14**: 68-79.

Kramarova NA, Frith SM, Bhartia PK, McPeters RD, Taylor SL, Fisher BL, Labow GJ, DeLand MT. 2013. Validation of ozone monthly zonal mean profiles obtained from the version 8.6 Solar Backscatter Ultraviolet algorithm. *Atmospheric Chemistry and Physics* **13**: 6887-6905.

Kyrölä E, Laine M, Sofieva V, Tamminen J, Pälvärinta S-M, Tukiainen S, Zawodny J, Thomason L. 2013. Combined SAGE II - GOMOS ozone profile data set 1984-2011 and trend analysis of the vertical distribution of ozone. *Atmospheric Chemistry and Physics* **13**: 10645-10658.

Lacis A, Hansen J. 1974. A parameterization for the absorption of solar radiation in the Earth's atmosphere. *Journal of the Atmospheric Sciences* **31**: 118-133.

Lean J. 2000. A decadal solar effect in the evolution of the Sun's spectral irradiance since the Maunder Minimum. *Geophysical Research Letters* **27**: 2425-2428, doi:10.1029/2000GL000043.

Lean J, Beer J, Bradley R. 1995. Reconstruction of solar irradiance since 1610: Implications for climate change. *Geophysical Research Letters* **22**: 3195–3198, doi:10.1029/2005GL025342.

Lee H, Smith AK. 2003. Simulation of the combined effects of solar cycle, quasi-biennial oscillation, and volcanic forcing on stratospheric ozone changes in recent decades. *Journal of Geophysical Research: Atmospheres* **108**: 4049, doi:10.1029/2001JD001503.

Madronich S, Flocke S. 1998. The role of solar radiation in atmospheric chemistry. In: *Handbook of Environmental Chemistry*, P. Boule, ed., Springer-Verlag, 1-26.

Marsh DR, Mills MJ, Kinnison DE, LaMarque J-F, Calvo N, Polvani L. 2013. Climate change from 1850 to 2005 simulated in CESM1(WACCM). *Journal of Climate* **26**: 7372-7391.

Matthes K, Kuroda Y, Kodera K, Langematz U. 2006. Transfer of the solar signal from the stratosphere to the troposphere: Northern winter. *Journal of Geophysical Research: Atmospheres* **111**: D06108, doi:10.1029/2005JD006283.

McCormick MP, Zawodny J, Veiga R, Larsen J, Wang PH. 1989. An overview of SAGE I and II ozone measurements. *Planetary and Space Science* **37**: 1567-1586.

McPeters RD, Bhartia PK, Haffner D, Labow GJ, Flynn L. 2013. The v8.6 SBUV ozone data record: An overview. *Journal of Geophysical Research: Atmospheres* **118**: doi:10.1002/jgrd.50597.

Meehl GA, Arblaster JM, Matthes K, Sassi F, van Loon H. 2009. Amplifying the Pacific climate system response to a small 11-year solar cycle forcing. *Science* **325**: 1114-1118.

Minschwaner K, Siskind D. 1993. A new calculation of nitric oxide photolysis in the stratosphere, mesosphere, and lower thermosphere. *Journal of Geophysical Research Atmospheres* **98**: 20401-20412.

Misios S, Mitchell DM, Gray LJ, Tourpali K, Matthes K, Hood L, Schmidt H, Chiodo G, Thiéblemont R, Rozanov E, Krivolutsky A. 2014. Solar signals in CMIP-5 simulations: Effects of atmosphere-ocean coupling. *Quarterly Journal of the Royal Meteorological Society* submitted.

Mitchell DM, Misios S, Gray LJ, Tourpali K, Matthes K, Hood L, Schmidt H, Chiodo G, Thiéblemont R, Rozanov E, Krivolutsky A. 2014a. Solar signals in CMIP-5 simulations: The stratospheric pathway. *Quarterly Journal of the Royal Meteorological Society* submitted.

Mitchell DM, Gray LJ, Fujiwara M, Hibino T, Anstey JA, Ebisuzaki W, Harada Y, Long C, Misios S, Stott P, Tan D. 2014b. Signatures of naturally induced variability in the atmosphere using multiple reanalysis datasets. *Quarterly Journal of the Royal Meteorological Society* submitted.

Randel WJ, Wu F. 2007. A stratospheric ozone profile data set for 1979-2005: Variability, trends, and comparisons with column ozone data. *Journal of Geophysical Research: Atmospheres* **112**: D06313, doi:10.1029/2006JD007339.

Remsberg EE. 2014. Decadal-scale responses in middle and upper stratospheric ozone from SAGE II version 7 data. *Atmospheric Chemistry and Physics* **14**: 1039-1053.

Russell GL, Miller JR, Rind D. 1995. A coupled atmosphere-ocean model for transient climate change studies. *Atmosphere-Ocean* **33**: 683-730.

Sato M, Hansen J, McCormick J, Pollack J. 1993. Stratospheric aerosol optical depths, 1850-1990. *Journal of Geophysical Research* **98**(D12): 22987-22994.

Schmidt GA, Kelley M, Nazarenko L, Ruedy R, Russell GL, Aleinov, Bauer M, Bauer SE, Bhat MK, Bleck R, et al. 2014. Configuration and assessment of the GISS ModelE2 contributions to the CMIP5 archive. *Journal of Advances in Modeling Earth Systems* **6**: 141-184.

Sekiguchi M, Nakajima T. 2008. A k-distribution based radiation code and its computational optimization for an atmospheric general circulation model. *Journal of Quantitative Spectroscopy and Radiative Transfer* **109**: 2779-2793.

Shapiro AV, Rozanov EV, Shapiro AI, Egorova TA, Harder J, Weber M, Smith AK, Schmutz W, Peter T. 2013. The role of the solar irradiance variability in the evolution of the middle atmosphere during 2004-2009. *Journal of Geophysical Research Atmospheres* **118**: 3781-3793, doi:10.1002/jgrd.50208.

Shibata K, Deushi M, Sekiyama TT, Yoshimura H. 2005. Development of an MRI chemical transport model for the study of stratospheric chemistry. *Papers in Geophysics and Meteorology* **55**: 75-119.

Shindell DT, Pechony O, Voulgarakis Z, Faluvegi G, Nazarenko L, Lamarque J-F, Bowman K, Milly G, Kovari B, Ruedy R, Schmidt GA. 2013. *Atmospheric Chemistry and Physics* **13**: 2653-2689.

Solomon S, Portmann RW, Garcia RR, Thomason LW, Poole LR, McCormick MP. 1996. The role of aerosol variations in anthropogenic ozone depletion at northern midlatitudes. *Journal of Geophysical Research: Atmospheres* **101**: 6713-6727.

Soukharev BE, Hood L. 2006. Solar cycle variation of stratospheric ozone: Multiple regression analysis of long-term satellite data sets and comparisons with models. *Journal of Geophysical Research: Atmospheres* **111**: D20314, doi:10.1029/2006JD007107.

SPARC-CCMVal 2010. SPARC Report on the Evaluation of Chemistry-Climate Models, in *SPARC Report No. 5, WCRP-132, WMO/TD-No. 1526*, edited by V. Eyring, T. G. Shepherd, and D. W. Waugh.

Sun S, Bleck R. 2006. Multi-century simulations with the coupled GISS-HYCOM climate model: Control experiments. *Climate Dynamics* **26**: 407-428.

Taylor KE, Stouffer RJ, Meehl GA. 2012. An overview of CMIP-5 and the experiment design. *Bulletin of the American Meteorological Society* **93**: 485-498.

Tiao G, Reinsel G, Xu D, Pedrick J, Zhu X, Miller A, DeLuisi J, Mateer C, Wuebbles D. 1990. Effects of autocorrelation and temporal sampling schemes on estimates of trend and spatial correlation. *Journal of Geophysical Research: Atmospheres* **95**: 20507-20517.

Viereck R, Puga L. 1999. The NOAA MG II core-to-wing solar index: Construction of a 20-year time series of chromospheric variability from multiple satellites. *Journal of Geophysical Research: Atmospheres* **104**: 9995-10005.

Wang YM, Lean J, Sheeley Jr N. 2005. Modeling the sun's magnetic field and irradiance since 1713. *The Astrophysical Journal* **625**: 522-538.

Watanabe S, Hajima T, Sudo K, Nagashima T, Takemura T, Okajima H, Nozawa T, Kawase H, Abe M, Yokohata T, et al. 2011. MIROC-ESM 2010: Model description and basic results of CMIP5-20c3m experiments. *Geoscientific Model Development* **4**: 845-872.

Woods TN. 2012. Solar irradiance variability: Comparisons of observations over solar cycles 21-24. In: *EGU General Assembly Conference Abstracts*, edited by Abbasi A, Giesen N. **14**: 1520.

World Meteorological Organization. 2007. *Scientific Assessment of Ozone Depletion: 2006*. World Meteorological Organization, Global Ozone Research and Monitoring Project, Report No. 50.

Yukimoto S, Kodera K. 2007. Annular modes forced from the stratosphere and interactions with the oceans. *Journal of the Meteorological Society of Japan* **85**: 943-952.

Yukimoto S, Yoshimura H, Hosaka M, Sakami T, Tsujino H, Hirabara M, Takana TY, Deushi M, Obata A, Nakano H, et al. 2011. Meteorological Research Institute-Earth System Model Version 1 (MRI-ESM1) - Model Description. *Technical Reports of the Meteorological Research Institute No. 64*, Meteorological Research Institute, Tsukuba City, Japan.

Yukimoto S, Adachi Y, Hosaka M, Sakami T, Youshimura H, Hirabara M, Tanaka T, Shindo S, Tsujino H, Deushi M et al. 2012. A new global climate model of the Meteorological Research Institute: MRI-CGCM3 Model description and basic performance. *Journal of the Meteorological Society of Japan* **90A**: 23-64, doi:10.2151/jmsj.2012-A02.

Model	Ensemble Members	# of Bands	Vertical Resolution*	Horizontal Resolution	QBO?	Reference
CESM1-WACCM	4	19	2-3 km	$1.9^\circ \times 2.5^\circ$	Nudged	Marsh et al. 2013
MIROC-ESM-CHEM	1	23	$\sim$ 1.1 km	$2.8^\circ \times 2.8^\circ$	Spontaneous	Watanabe et al. 2011
MRI-ESM1	1	22	$\sim$ 2.5 km	$\sim 1.1^\circ$	None	Yukimoto et al. 2010
GFDL-CM3	5	18	2-3 km	$\sim 2^\circ$	None	Donner et al. 2011
GISS-E2-H	5	6	$\sim$ 2 km	$2^\circ \times 2.5^\circ$	None	Shindell et al. 2013
GISS-E2-R	5	6	$\sim$ 2 km	$2^\circ \times 2.5^\circ$	None	Shindell et al. 2013

* Value in the upper stratosphere near 40 km altitude.

Table 1: High-Top CMIP-5 Models With Interactive Chemistry

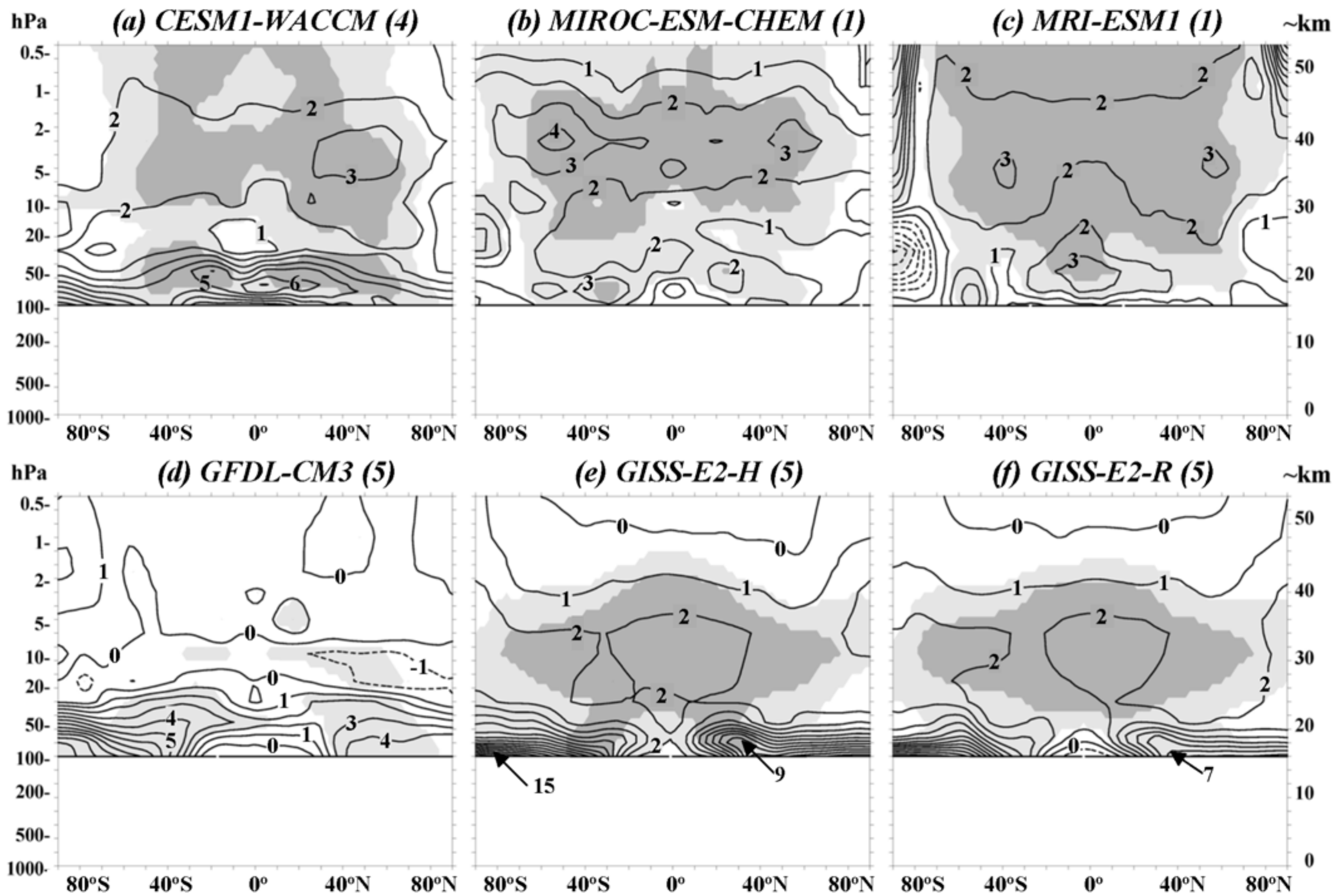

Figure 1. Annual and zonal mean ozone per cent change (max - min) over the 1979-2005 period for the 6 high-top models with interactive chemistry (see the text). Dark (light) shading indicates statistical significance at the 2 (1) sigma level. The contour interval is 1%.

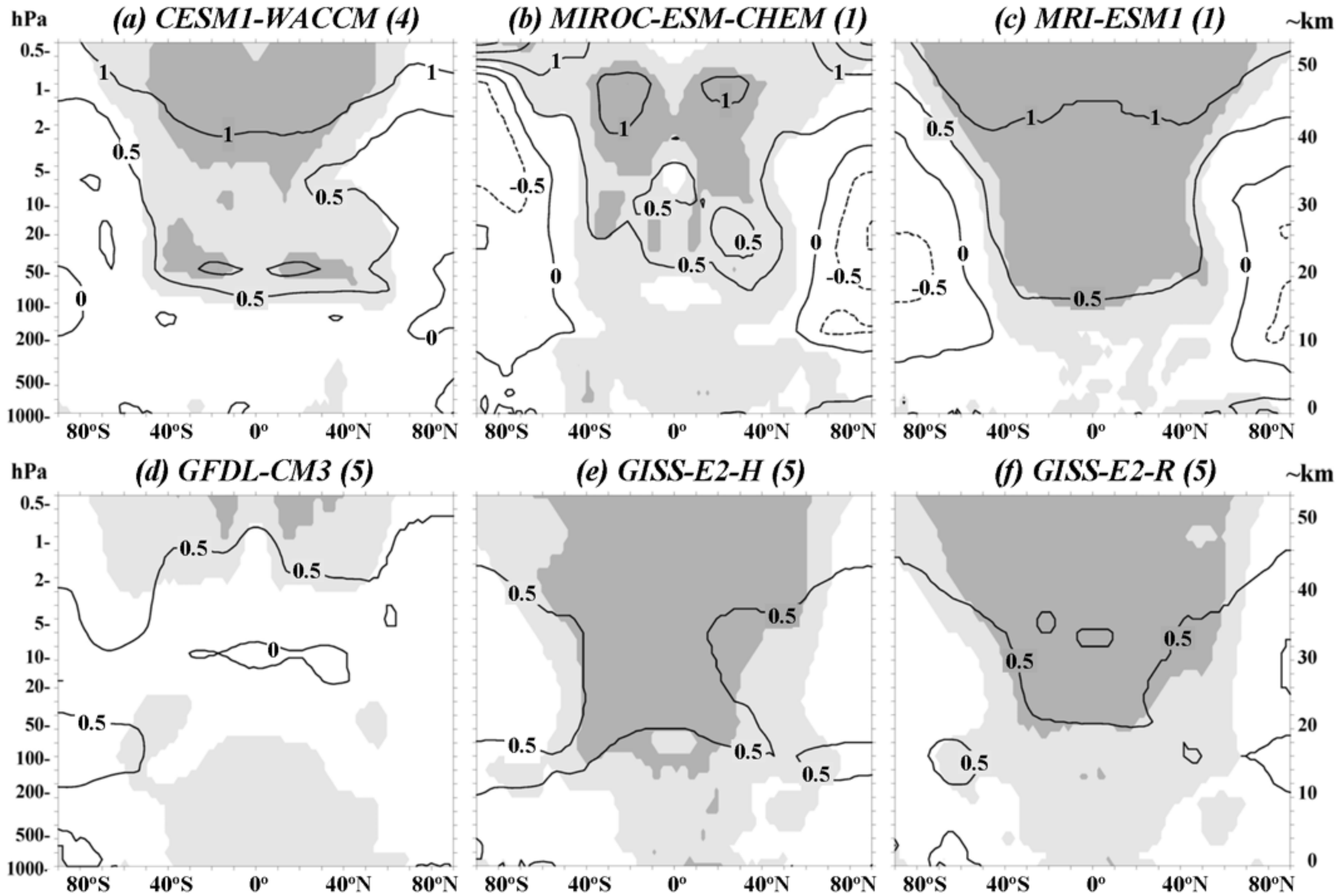

Figure 2. Same format as Figure 1 but for the annual and zonal mean temperature change (max - min) over the 1979-2005 period.

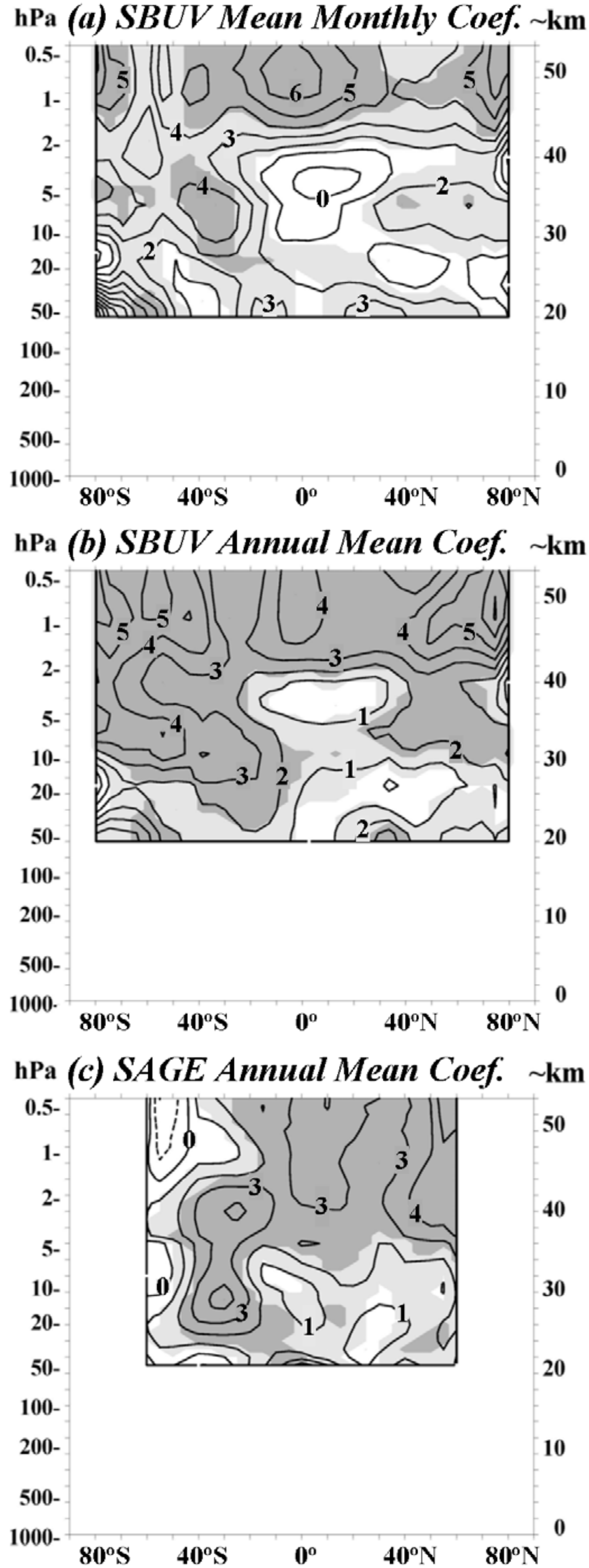

Figure 3. (a) Annually averaged monthly ozone change (max - min) for the Version 8 merged SBUV ozone data over the 1979-2003 period; (b) Same as (a) but for the annual mean ozone change; (c) Annual mean ozone change for the Version 6 SAGE II data set over the 1985-2005 period.

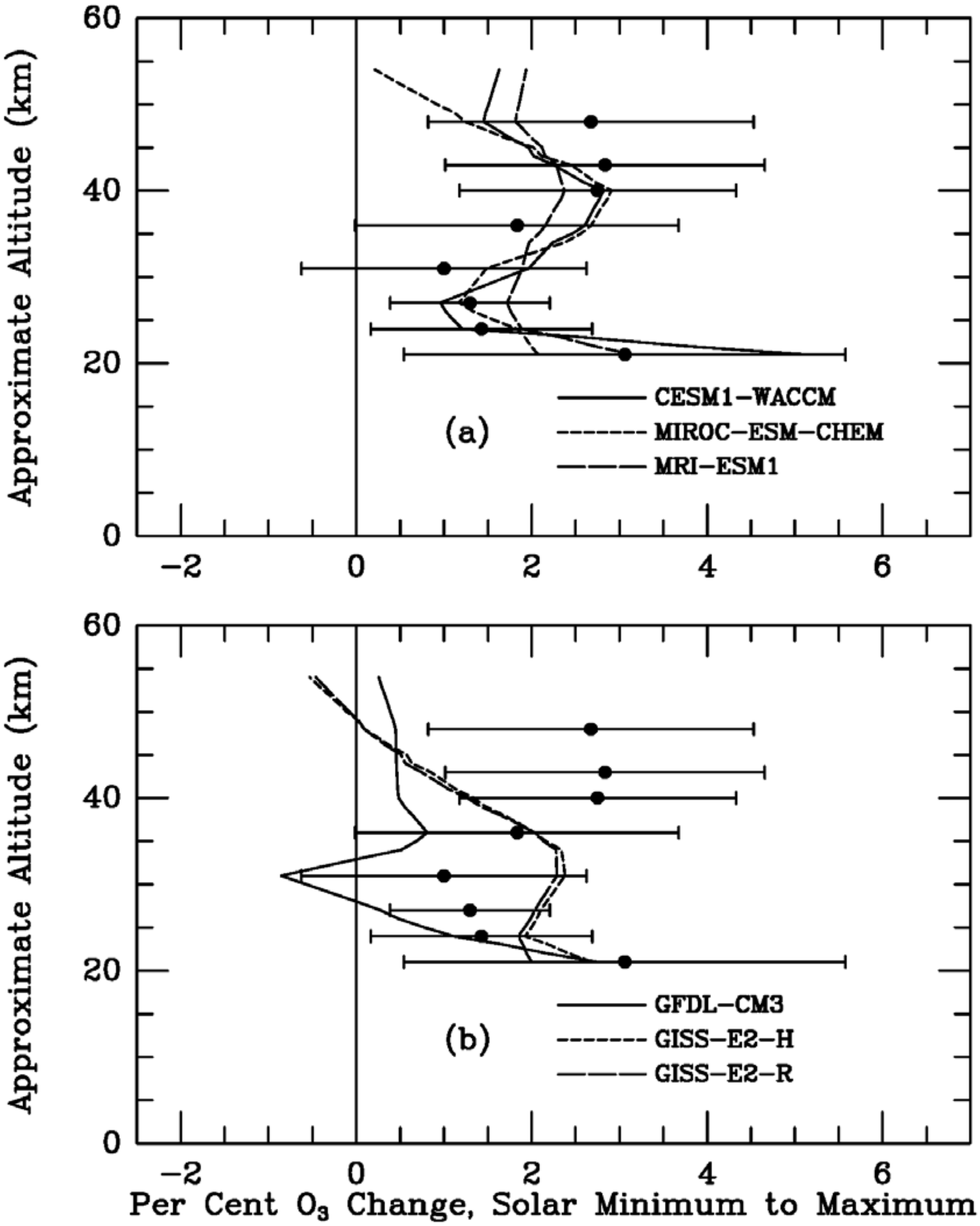

Figure 4. Comparison of tropical (25^{o}S to 25^{o}N) averages of SAGE II annual mean ozone solar regression coefficients (solid circles with 2σ error bars) with similar averages of the annually averaged model solar regression results of Figure 1. The top panel (a) is for the three models with a substantial upper stratospheric ozone response while the bottom panel (b) is for the remaining three models.

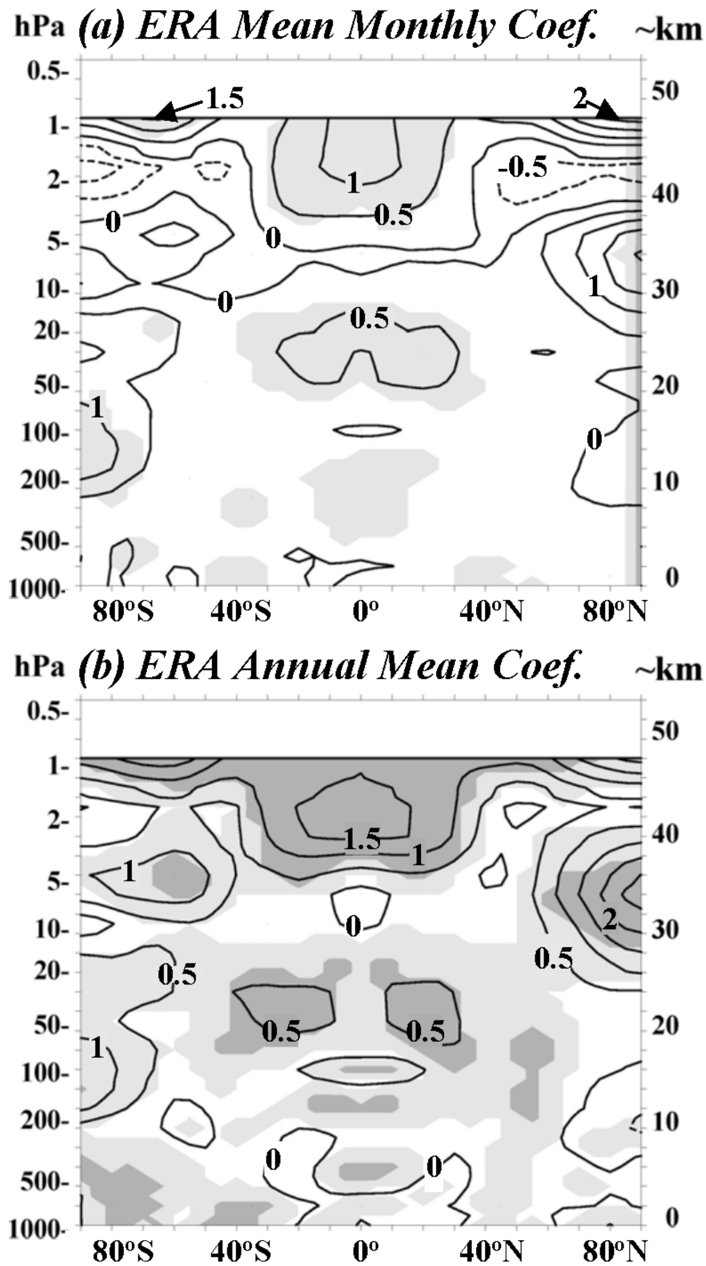

Figure 5. (a) Annually averaged monthly temperature change (max - min) over the 1979-2012 period for the ERA Interim reanalysis data set after adjustments for offset step changes in the upper stratosphere; (b) Same as (a) but for the annual mean temperature change with each monthly temperature anomaly considered as an independent data point.

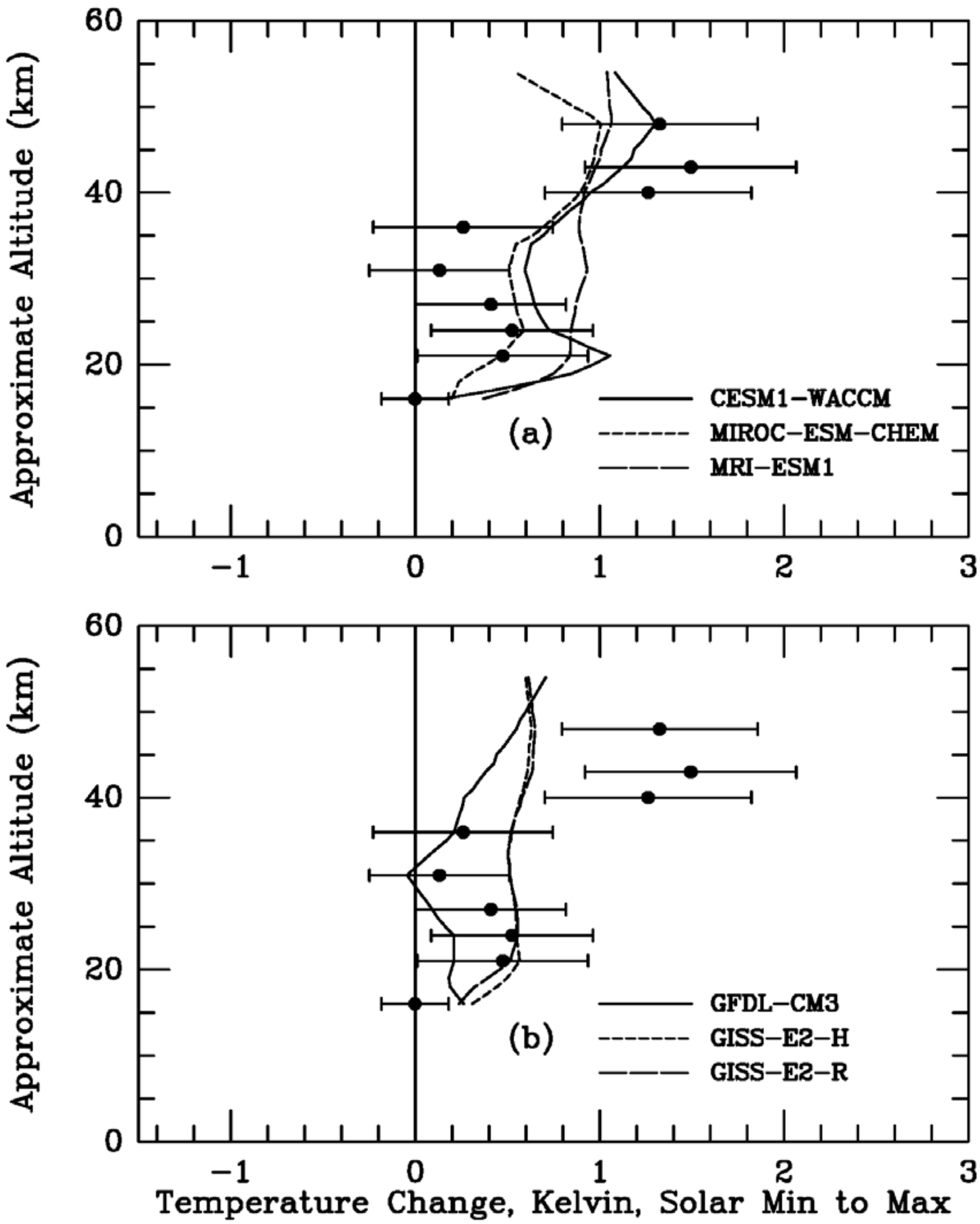

Figure 6. Comparison of tropical (25°S to 25°N) averages of adjusted ERA Interim annual mean temperature solar regression coefficients (solid circles with 2σ error bars) with similar averages of the annually averaged model solar regression results of Figure 2. The top panel (a) is for the three models with a substantial upper stratospheric ozone response while the bottom panel (b) is for the remaining three models.

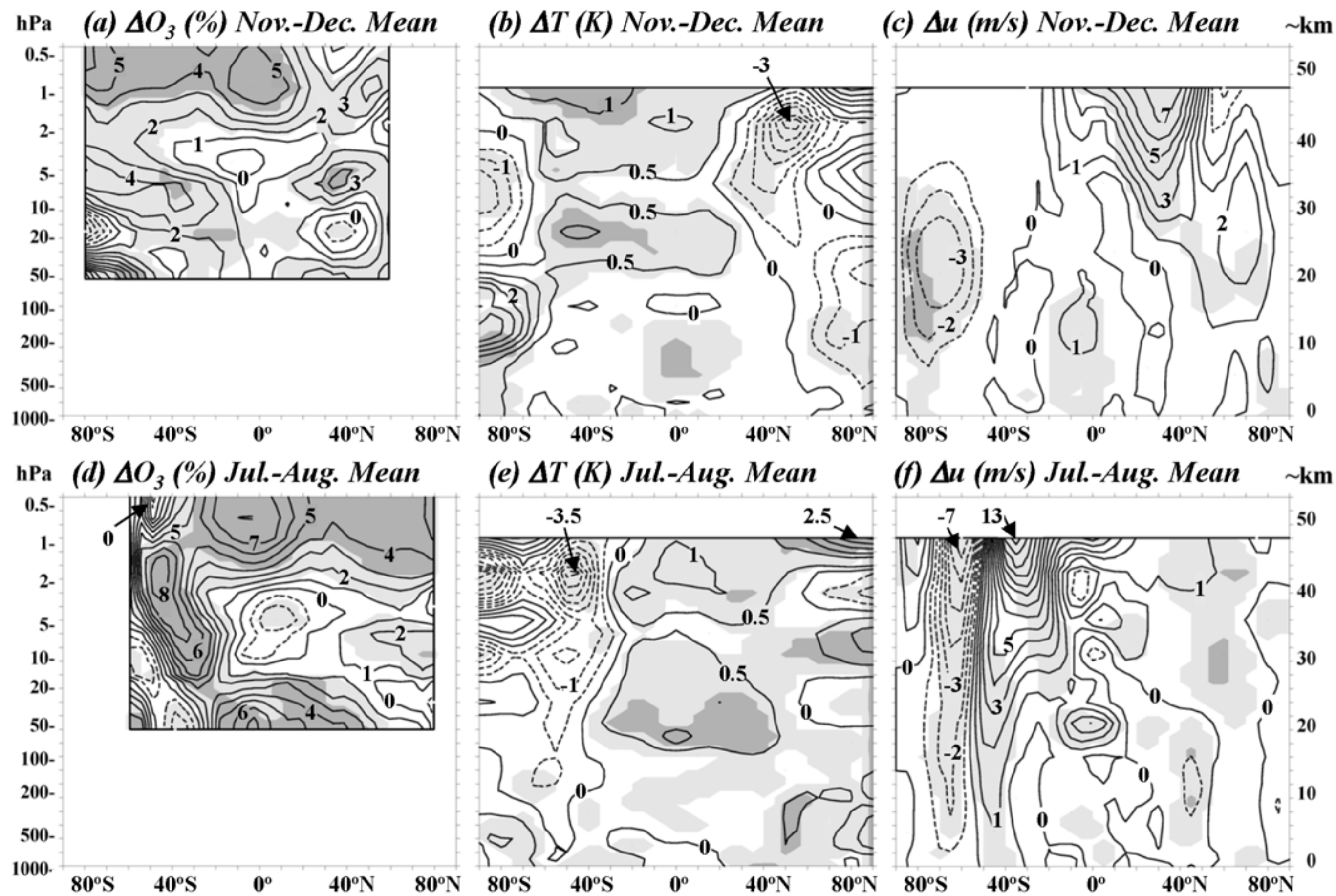

Figure 7. Observationally estimated solar cycle change (max - min) in zonal mean ozone, temperature, and zonal wind during early northern winter (top panel) and middle southern winter (bottom panel). See the text. The contour interval is 1% for ozone, 0.5 K for temperature, and 1 m/s for zonal wind.

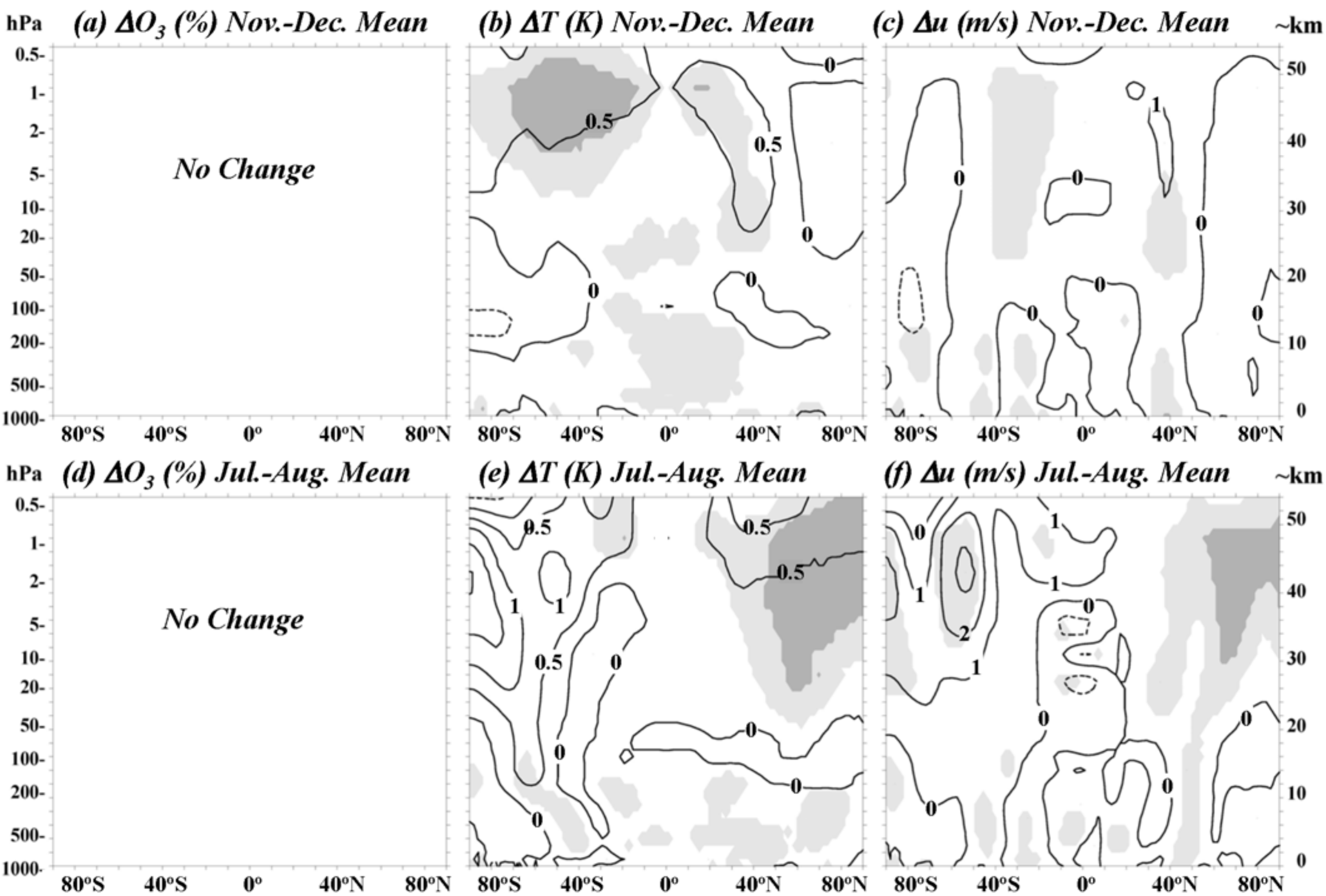

Figure 8. Solar cycle change (max - min) in zonal mean temperature and zonal wind during early northern winter (top panel) and middle southern winter (bottom panel) for the MIROC-ESM model (mean of 3 ensemble members) over the 1979-2005 period. This model used a prescribed ozone database that did not include a representation of the solar cycle. The contour interval is 0.5 K for temperature, and 1 m/s for zonal wind.

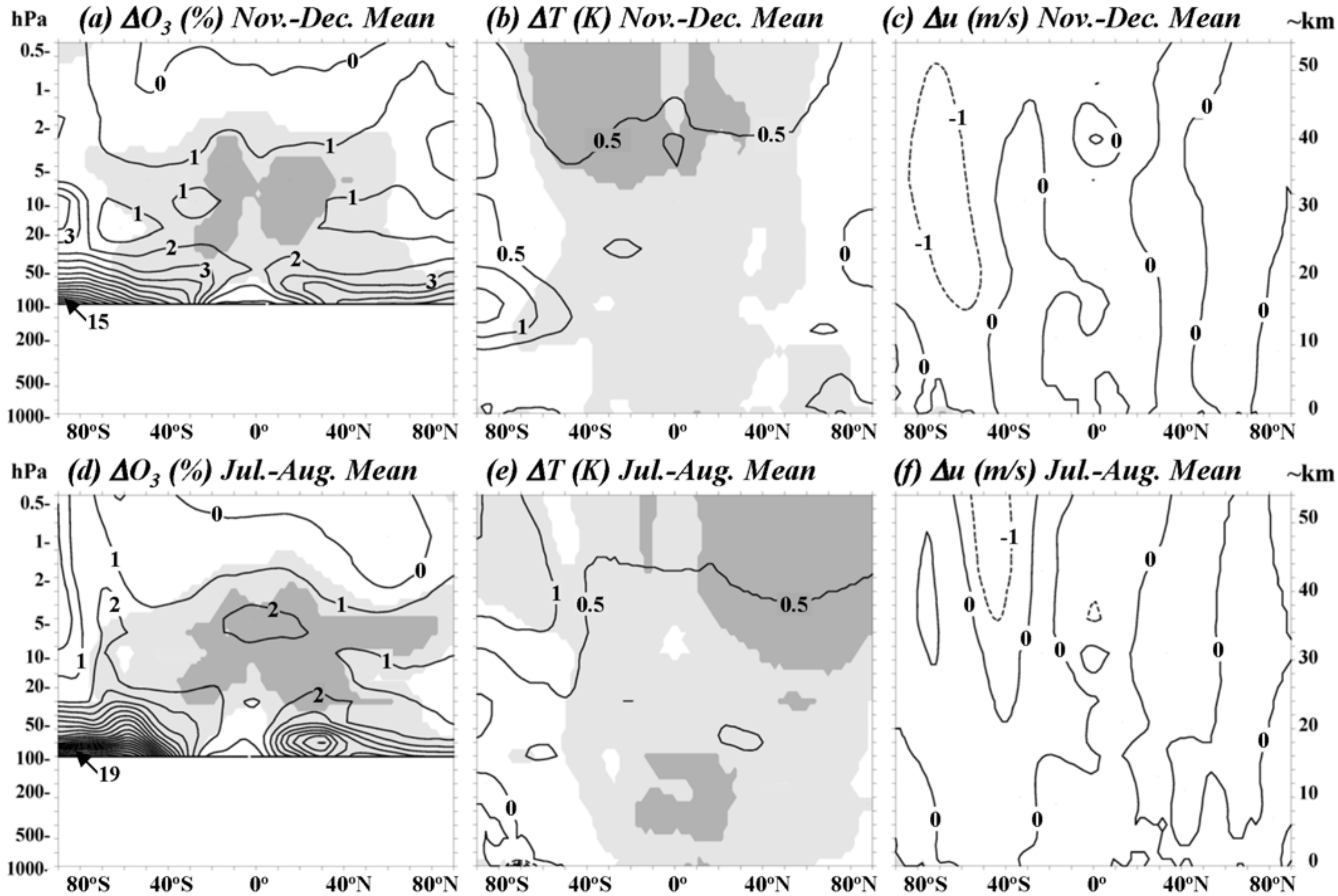

Figure 9. Mean solar cycle change (max - min) in zonal mean ozone, temperature, and zonal wind during early northern winter (top panel) and middle southern winter (bottom panel) for the three interactive chemistry models with relatively weak upper stratospheric ozone responses (GFDL-CM3, GISS-E2-H, and GISS-E2-R). The contour interval is 1% for ozone, 0.5 K for temperature, and 1 m/s for zonal wind.

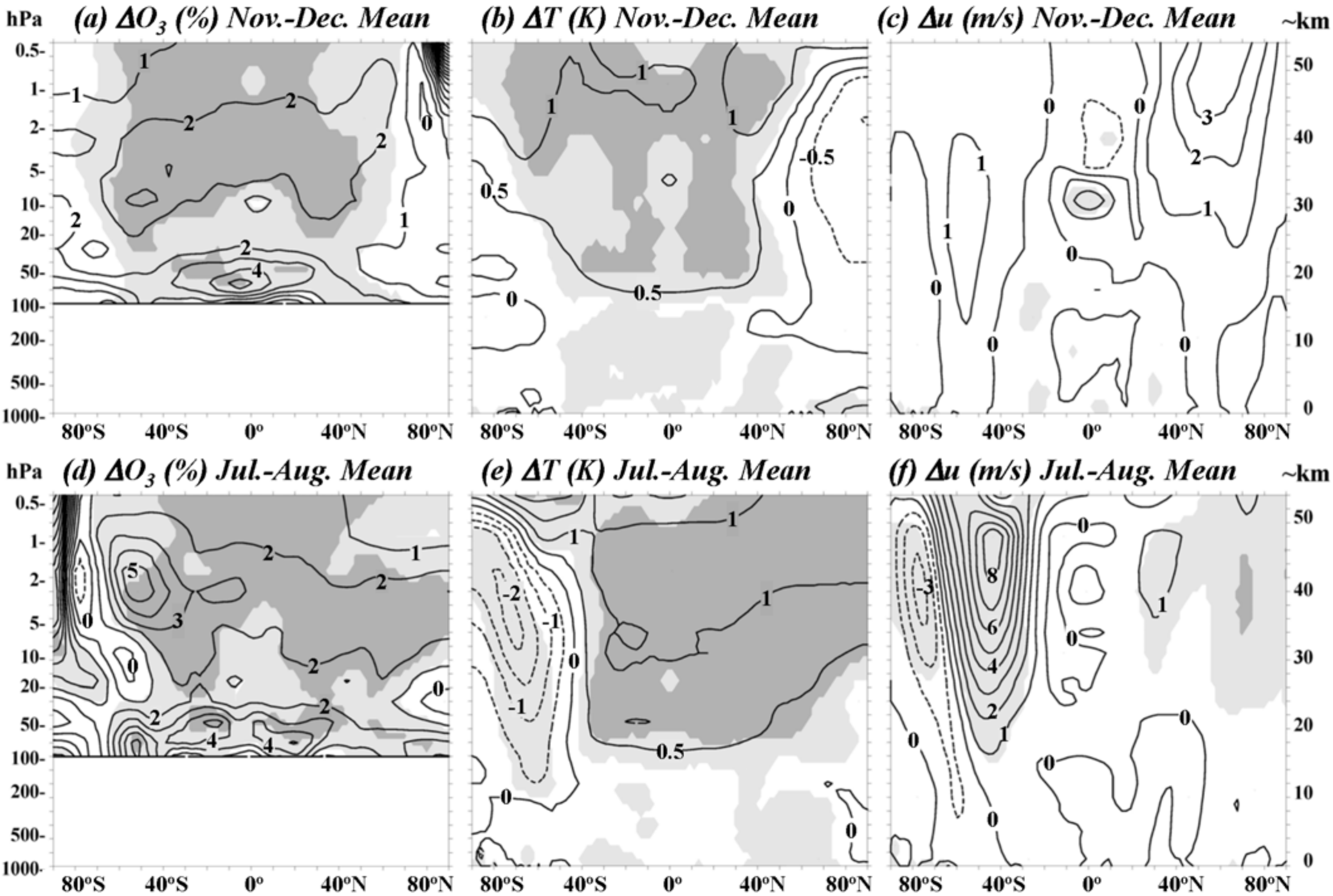

Figure 10. As in Figure 9 but for the three interactive chemistry models with relatively strong upper stratospheric ozone responses (CESM1-WACCM, MIROC-ESM-CHEM, and MRI-ESM1).

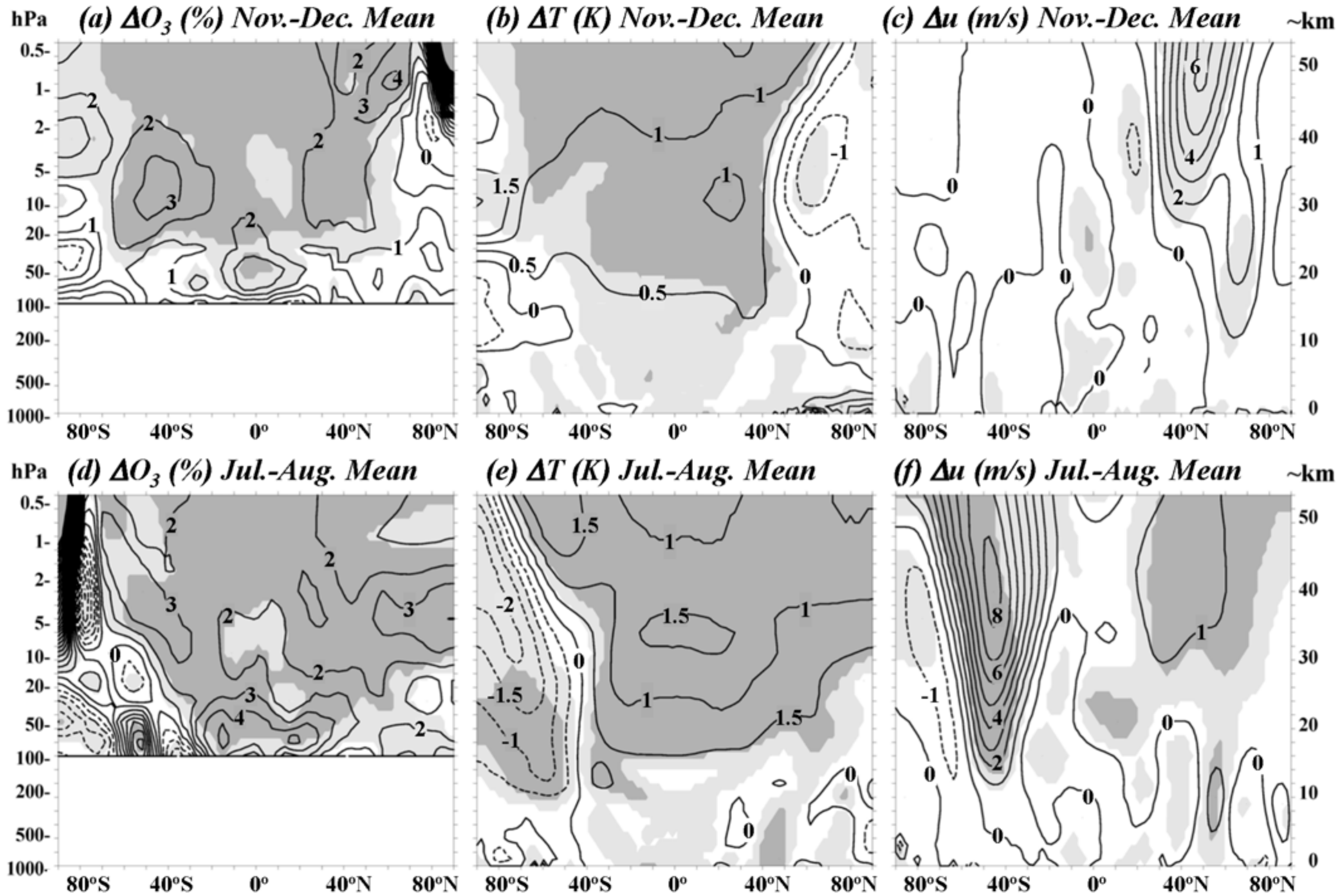

Figure 11. As in Figures 9 and 10 but for the single MRI-ESM1 simulation over the 1979-2005 period.

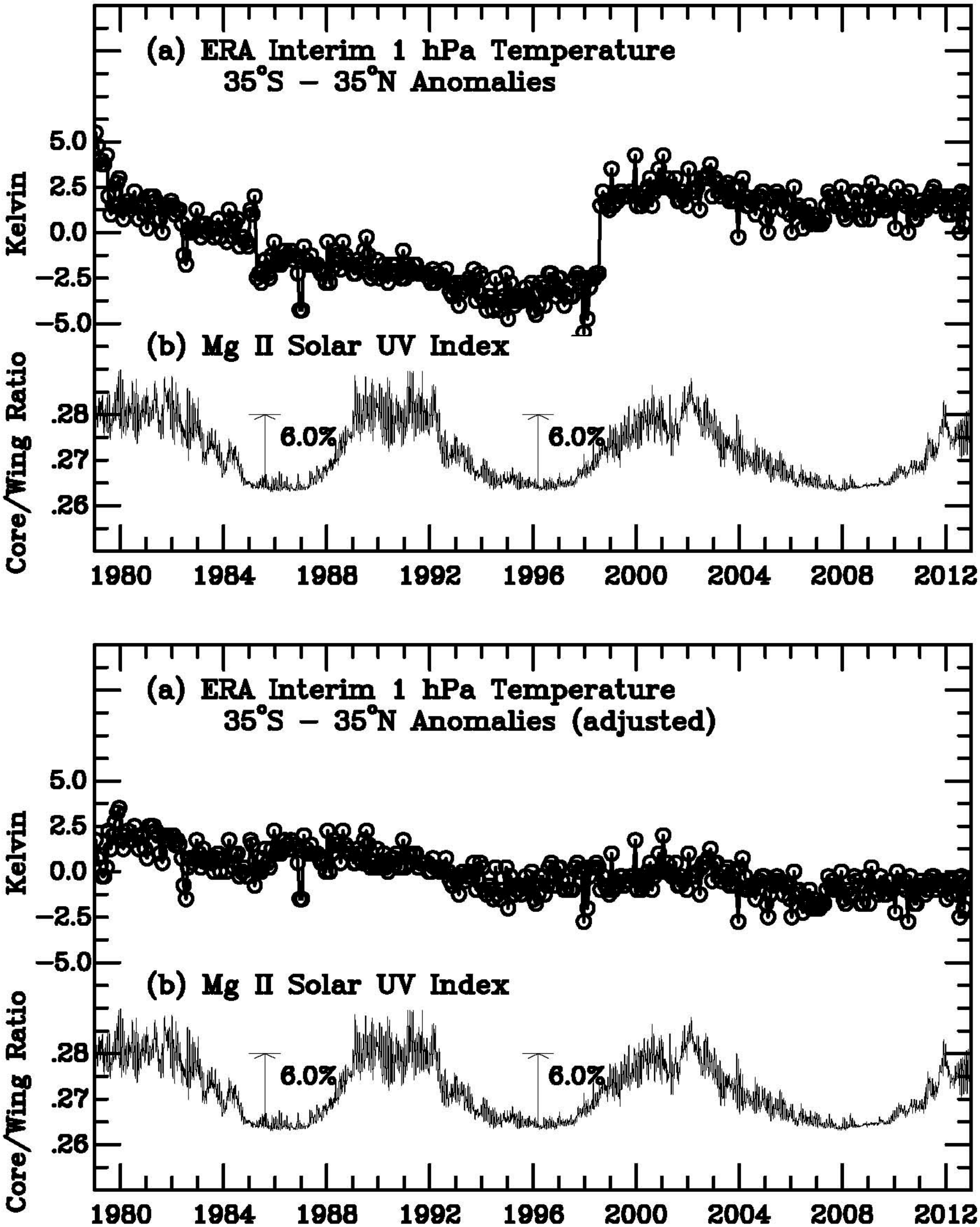

Figure A1. Top panel: (a) Area-weighted average over low latitudes of the ERA Interim 1 hPa monthly temperature anomalies (deviations from long-term monthly means); (b) The Mg II core-to-wing ratio solar UV index. Bottom Panel: Same format as top panel but after offset adjustments are applied to the data (see the text).